


















Extrapolation of Type Ia Supernova Spectra into the Near-Infrared Using PCA

ANTHONY BURROW ¹, E. BARON ^{2,3,1}, CHRISTOPHER R. BURNS ⁴, ERIC Y. HSIAO ⁵, JING LU ⁶,
CHRIS ASHALL ⁷, PETER J. BROWN ⁸, JAMES M. DERKACY ⁷, G. FOLATELLI ^{9,10,11}, LLUÍS GALBANY ¹²,
P. HOEFLICH ⁵, KEVIN KRISCIUNAS ⁸, N. MORRELL ¹³, M. M. PHILLIPS ¹³, BENJAMIN J. SHAPPEE ¹⁴,
MAXIMILIAN D. STRITZINGER ¹⁵ AND NICHOLAS B. SUNTZEFF ⁸

- ¹Homer L. Dodge Department of Physics and Astronomy, University of Oklahoma, Rm 100 440 W. Brooks, Norman, OK 73019-2061
²Planetary Science Institute, 1700 East Fort Lowell Road, Suite 106, Tucson, AZ 85719-2395 USA
³Hamburger Sternwarte, Gojenbergsweg 112, 21029 Hamburg, Germany
⁴Observatories of the Carnegie Institution for Science, 813 Santa Barbara St., Pasadena, CA 91101, USA
⁵Department of Physics, Florida State University, Tallahassee, FL 32306, USA
⁶Department of Physics & Astronomy, Michigan State University, East Lansing, MI, USA
⁷Department of Physics, Virginia Tech, 850 West Campus Drive, Blacksburg VA, 24061, USA
⁸George P. and Cynthia Woods Mitchell Institute for Fundamental Physics and Astronomy, Department of Physics and Astronomy, Texas A&M University, College Station, TX 77843, USA
⁹Instituto de Astrofísica de La Plata (IALP), CONICET, Paseo del Bosque S/N, B1900FWA La Plata, Argentina
¹⁰Facultad de Ciencias Astronómicas y Geofísicas Universidad Nacional de La Plata, Paseo del Bosque, B1900FWA, La Plata, Argentina
¹¹Kavli Institute for the Physics and Mathematics of the Universe (WPI), The University of Tokyo, Kashiwa, 277-8583 Chiba, Japan
¹²Departamento de Física Teórica y del Cosmos, Universidad de Granada, E-18071 Granada, Spain
¹³Las Campanas Observatory, Carnegie Observatories, Casilla 601, La Serena, Chile
¹⁴Institute for Astronomy, University of Hawai'i at Manoa, 2680 Woodlawn Dr., Hawai'i, HI 96822, USA
¹⁵Department of Physics and Astronomy, Aarhus University, Ny Munkegade 120, DK-8000 Aarhus C, Denmark.

(Received January 26, 2024; Revised March 21, 2024; Accepted April 4, 2024)

Submitted to ApJ

ABSTRACT

We present a method of extrapolating the spectroscopic behavior of Type Ia supernovae (SNe Ia) in the near-infrared (NIR) wavelength regime up to 2.30 μm using optical spectroscopy. Such a process is useful for accurately estimating K-corrections and other photometric quantities of SNe Ia in the NIR. Principal component analysis is performed on data consisting of Carnegie Supernova Project I & II optical and near-infrared FIRE spectra to produce models capable of making these extrapolations. This method differs from previous spectral template methods by not parameterizing models strictly by photometric light-curve properties of SNe Ia, allowing for more flexibility of the resulting extrapolated NIR flux. A difference of around -3.1% to -2.7% in the total integrated NIR flux between these extrapolations and the observations is seen here for most test cases including Branch core-normal and shallow-silicon subtypes. However, larger deviations from the observation are found for other tests, likely due to the limited high-velocity and broad-line SNe Ia in the training sample. Maximum-light principal components are shown to allow for spectroscopic predictions of the color-stretch light-curve parameter, s_{BV} , within approximately ± 0.1 units of the value measured with photometry. We also show these results compare well with NIR templates, although in most cases the templates are marginally more fitting to observations, illustrating a need for more concurrent optical+NIR spectroscopic observations to truly understand the diversity of SNe Ia in the NIR.

1. INTRODUCTION

Type Ia supernovae (SNe Ia) are broadly useful tools in cosmology that provide insight into the nature of dark energy (Riess et al. 1998; Perlmutter et al. 1999; Brout et al. 2019a,b) as extragalactic distance indicators. This comes as a result of their standardizable properties; they have been made correctable standard candles in the past by the use of their light-curve shapes that have been quantified using empirical parameters such as the decline rate, $\Delta m_{15}(B)$ (e.g. Phillips 1993; Hamuy et al. 1996), or stretch-like quantities such as color-stretch, s_{BV} (Burns et al. 2014). Parameterizing these light-curves facilitates the estimation of the distance modulus and host reddening through well-known correlations between the intrinsic maximum luminosities of SNe Ia and their light-curve shapes (Phillips 1993; Riess et al. 1996; Phillips et al. 1999) and colors (Tripp 1998).

However, because the precision with which cosmological properties may be deduced is so dependent on light-curves, the time-evolution of SNe Ia up to around 40 days past maximum light must be fully understood to reduce the uncertainty in these cosmological properties, including Hubble residuals. Unfortunately, the parent systems of individual SNe Ia remain unclear; neither the progenitor system nor the explosion mechanism are generally agreed upon within the community (see, e.g., Maoz et al. 2014; Jha et al. 2019, for recent reviews). This is because the carbon-oxygen white dwarfs that explode and produce the spectra of the SNe Ia we observe are not observable pre-explosion. As such, through the ever-expanding collection of recent observations obtained, a common approach to deducing progenitor and explosion channels is by statistical analysis to seek correlations in both photometric and spectroscopic indicators in samples of SNe Ia. As more observations are obtained, the uncertainties of subtypes of SNe Ia will be reduced, allowing for better methods of modeling individual SNe Ia, which may improve their use as cosmological distance indicators and provide more insight into stellar evolution as a whole.

Recently, the behavior of SN Ia spectra have been studied by the use of advanced statistical methods and machine-learning techniques. As sample sizes of observed SNe Ia are fairly low and time-dependent, it becomes difficult and even inadvisable to make use of methods such as neural networks in most cases. However, one approach that handles this limitation relatively well due to its simplicity is principal component analysis (PCA; Pearson 1901). PCA is a process of dimensionality reduction that is used to describe the highest degrees of variation in a given sample. This is done by algorithmically calculating a set of basis eigenvectors — or principal components (PCs) — that iteratively de-

scribe the most variation in the sample of data along each subsequent PC axis.

PCA has been employed to study the diversity of SNe Ia many times in the recent past. SALT2 and SALT3 (Guy et al. 2007; Kenworthy et al. 2021) use a technique very similar to principal component decomposition in conjunction by including a reddening factor to constrain SN Ia diversity to two parameters. This allows for estimates of distance and photometric redshift as well as aiding in SN Ia spectroscopic line identification. SNEMO, an empirical principal-component model has been generated to describe three different levels of SN Ia diversity that is comparable to SALT2 (Saunders et al. 2018). PCA has also been useful in constructing spectral energy distribution (SED) templates to model the baseline spectroscopic behavior of various SNe Ia in both the optical and near-infrared (NIR) wavelength regimes (see, e.g., Hsiao et al. 2007; Hsiao 2009; Lu et al. 2023). These templates have been parameterized by stretch-like quantities such as $\Delta m_{15}(B)$ and s_{BV} , as well as relative phase in time to give them time dependence. By doing so, these templates provide a convenient inference of an SED that may be used to determine time-dependent K-corrections to observed photometry, which are required to correct observed photometry for host-galaxy redshift (Oke & Sandage 1968).

Our primary goal in this project is to employ the use of PCA to create time-dependent models that describe the variations observed in both optical and NIR spectra. In this way, it should be possible to provide optical spectroscopy of any SN Ia to a model and perform an extrapolation process that infers the spectroscopic behavior of that SN Ia at that phase in time in the NIR with some known uncertainty. This estimation could be used in a similar manner to templates — to estimate an SED in order to perform K-corrections and bolometric luminosity calculations at any point in time. This is especially useful as optical and NIR photometry of the same SN Ia are not often obtained simultaneously, particularly at early times.

This method is similar to the template method of inferring SNe Ia SEDs established by Hsiao et al. (2007) and extended by Lu et al. (2023), as both techniques make use of PCA to formulate a model. However, there are some key differences that should lead to different results. Most importantly, this work does not strictly parameterize models by s_{BV} , but rather by using abstract correlations in the spectroscopic features themselves. In general, this may allow more flexibility in how NIR behavior is predicted using optical information. It may be shown that light-curve shape cannot fully parameterize spectroscopic or photometric behavior; for example,

Burrow et al. (2020) show spectroscopically dissimilar SNe Ia that exhibit similar values of s_{BV} . SNe Ia with similar s_{BV} may also show variability of the secondary photometric light-curve peak seen in the NIR. Papadogiannakis et al. (2019) show varying levels of spread in the time of secondary maximum in the r and i bands for SNe Ia of similar s_{BV} . Therefore, it could be that not restricting the parameterization to s_{BV} may lead to different and possibly less uncertain results. In this way, this work is intended to be complementary to Lu et al. (2023) and provide an alternative outlook on the problem.

In addition, we also provide an analysis of how our results in the NIR may be influenced by the classification of a SN Ia established by Branch et al. (2006), which we refer to here as the Branch group classification. These Branch groups consist of the core-normal (CN), shallow-silicon (SS), broad-line (BL) and cool (CL) groups, and they have been shown to be robust in a detailed cluster analysis (Burrow et al. 2020). This classification system typically uses the measured pseudo-equivalent widths (pEWs) of Si II $\lambda 6355$ and Si II $\lambda 5972$ to classify SNe Ia into these four groups with what have been shown in previous studies to be unique spectroscopic and photometric properties. Photometrically, CNs and BLs have been shown to exhibit moderate values of s_{BV} , typically between $0.7 \lesssim s_{\text{BV}} \lesssim 1.1$, with clearly distinct Si II $\lambda 6355$ features between them (Burrow et al. 2020). SSs are usually associated with luminous, slow-declining SNe Ia, whereas CLs are dimmer and faster-declining. In this paper we examine how this optical classification scheme may relate to varying spectroscopic behavior seen in both the optical and the NIR using PCA.

In § 2, samples and selection criteria used to inform our PC models are discussed. In § 3, the methods used to create such models are discussed, as well as how these models are used along with a given optical SN Ia spectrum to predict its NIR spectrum. § 4 illustrates examples of the prediction process in different cases across relative time and for different classifications of SNe Ia. Finally in § 5, we discuss how the resulting PC eigenvectors may relate to the Branch groups as well as s_{BV} , and this extrapolation method is compared with spectral templates, both in spectroscopy and bolometric luminosity.

2. DATA

2.1. Data Source & Preprocessing

To represent the population of observable SN Ia spectra in both the optical and NIR, we make use of two different series of spectroscopic SNe Ia observations. The compiled spectra used in this project are described here.

The optical range of our data is provided by both Carnegie Supernova Project (CSP) I and II sets of spectra (Folatelli et al. 2010; Phillips et al. 2019; Hsiao et al. 2019; Burrow et al. 2020). This combined data set consists of spectra of 364 unique SNe Ia. The host redshift of SNe Ia in the CSP I data set lies in the range of $0.0037 < z < 0.0835$ (Krisciunas et al. 2017), and that of the CSP II set is within $0.03 < z < 0.10$ (Phillips et al. 2019).

The NIR component of the data used here is the same used by Lu et al. (2023), which was obtained using the Folded-port InfraRed Echellette (FIRE) in the high-throughput prism mode on the 6.5m Magellan Baade telescope. This instrument captures adequate signal at NIR wavelengths where considerable telluric absorption typically occurs, allowing for passable corrections to these regions, albeit still with relatively much noise and uncertainty. Acquiring as accurate spectroscopic measurements as possible of SNe Ia in these regions is crucial to achieving an SED suitable enough to calculate accurate bolometric light-curves and K-corrections. We choose to use this NIR set of spectra because this allows for consistency when comparing with NIR spectral templates of Lu et al. (2023), which is a goal of this project. In addition, the SNe Ia observed with FIRE were purposefully selected to have good overlap with many CSP II SNe Ia. These FIRE spectra include observations of 142 unique SNe Ia in total; however, using the same selection criteria as Lu et al. (2023), a total number of 94 SNe Ia are included in this NIR sample. These spectra typically capture up to around $2.4 \mu\text{m}$.

Every SN Ia used to inform models here also has optical photometric observations from CSP I & II (Krisciunas et al. 2017) such that light-curves have been fit to them using the light-curve-fitting software, SNooPy (Burns et al. 2014, 2018). This is so that photometric quantities required for this analysis, such as time of B -maximum and host reddening, are inferred for each SN Ia. There are 115 SNe Ia from CSP I with both spectra and these photometric quantities available, and similarly 161 SNe Ia from CSP II.

Ideally, each spectrum in the data set would be corrected such that its synthetic photometry would match the observed photometry at the same time. This may be done using SNooPy, for example, where a best-fit smooth basis spline with knots at the effective wavelength of each photometric filter is multiplied by the spectrum such that the result yields synthetic photometry closest to the observed values. However, as this project deals with both optical and NIR spectra, this means simultaneous values of optical and NIR photometry must be available for each spectrum used. Even

with light-curve interpolation for each individual filter, only a fraction of SNe Ia in our data set have optical photometry available to allow for this correction, and a much smaller fraction have NIR (Y , J , and H) photometry. Because of the non-parametric nature of the spline-based color-matching technique, the correction is useful for a study such as this only when both optical and NIR photometry are available. Therefore, the spectra used here are not corrected for observed photometry, and our models do not account for this source of variation. However, the CSP I spectra have been shown to give accurate optical colors (Stritzinger et al. 2023) including in $r - i$, which includes the wavelength region where the optical and NIR spectra are merged here. (Hsiao et al. 2019) also showed that the CSP II NIR colors obtained from synthetic photometry were accurate to 0.03 – 0.08 mag.

To eliminate as much other known, systematic variation in the training data sample as possible before the eigenvectors are calculated, some additional preliminary processing has been performed. Three optical telluric features at 5876–5910 Å, 6849–6929 Å, and 7576–7688 Å were removed from each spectrum. Then, each spectrum was put into the rest frame and corrected for Milky Way (MW) extinction using reddening estimates of Schlafly & Finkbeiner (2011) with $R_V = 3.1$ and a host-galaxy color-excess value $E(B - V)_{host}$ inferred by SNooPy. These corrections were performed using the CCM law given by Cardelli et al. (1989). Note that host-galaxy extinction is less certain than MW extinction, therefore some variability due to host extinction could be present in PCs described later in § 3.

2.2. Sample Selection

As discussed in § 1, the goal of this extrapolation method is to use the available data to train a time-dependent model that describes both optical and NIR spectroscopy. Rather than compiling all available observed spectra into a single model by the use of some interpolation technique such as Gaussian processes, we have chosen to generate multiple models, with each model representing SN Ia spectra at some point in time. Specifically, each model will represent an integer day past B -band maximum (i.e. day -1 , day $+0$, day $+1$, etc.). We chose to incorporate time-dependence in this way to eliminate possible bias; for example, two SNe Ia of different subtypes may appear spectroscopically similar in some aspects at different phases in time (e.g., Yarbrough et al. 2023). In doing this, the effects of time evolution should be minimally captured by our individual models. In addition, hereafter in this paper, maximum light will always refer to the time of B -band maximum.

The sample of spectra selected from our total data set for each individual model representing some time t is chosen in the following way. First, for every SN Ia that has spectra observed before and after t , we interpolate the spectra using Gaussian process regression (GPR) if there are enough spectra and there is an observed spectrum close enough to t . We find that 3–4 observed spectra within approximately -10 to $+50$ days of maximum light provide a good interpolation with low propagated uncertainties from the GPR if at least two of those observation times surround t — otherwise it would require extrapolation rather than interpolation. If the SN Ia is sparsely observed or is otherwise unable to be interpolated, we choose the spectrum observed closest to time t within -5 to $+10$ days relative to t . This window is asymmetric to allow for more spectra to lie within the window, while assuming observed spectra change more dynamically for the same SN Ia at earlier times. Although using such a large window may introduce some time evolution into the model, we find that this is favorable *in lieu* of the smaller sample sizes that a smaller window would generate. Larger sample sizes would produce smaller uncertainties, which are discussed in § 3.4.

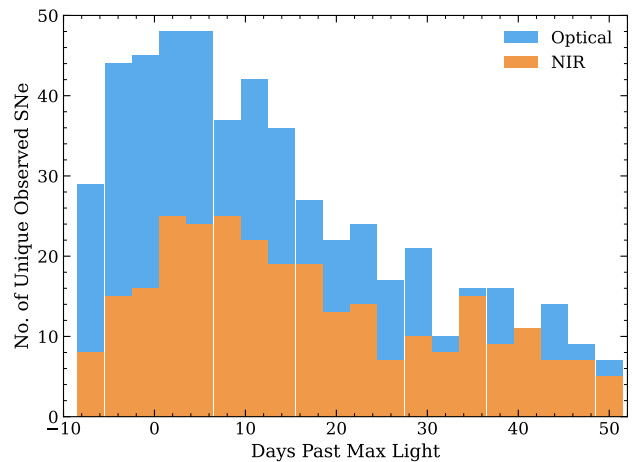


Figure 1. Bars here show the number of unique observed SNe Ia in the optical and NIR data sets as a function of time past B maximum in three-day bins.

To reiterate, small sample size is the primary difficulty in this analysis. To illustrate the optical and NIR data sets used, in Figure 1 we show a histogram of the number of unique SNe Ia from each data set with at least one observation within the given bins, which are three days wide, ranging from -10 to $+50$ days relative to maximum light. This only accounts for those we use for the analysis; that is, those that have had light-curves fit, etc. Both samples contain more observations at times near

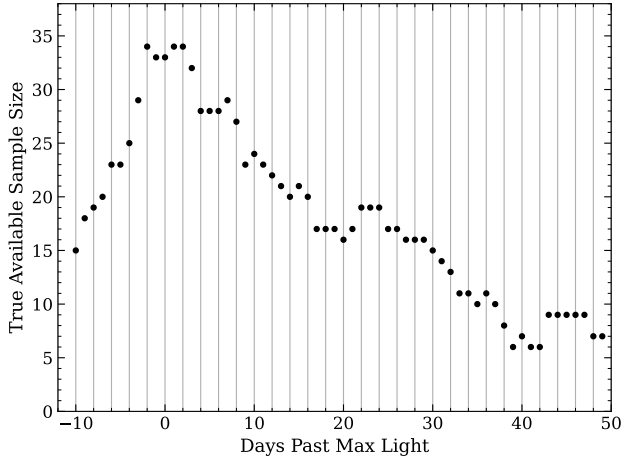


Figure 2. The true available sample size for our models as a function of time, accounting for both optical and NIR spectra eligible to have a representative spectrum for that time (described in § 2.2).

maximum light, implying that our models will be more accurate when used to extrapolate spectra observed near the epoch of maximum light. This may be more useful as it is often more difficult to arrange observations of the same SNe Ia concurrently in the optical and NIR at earlier times, and the early phase characterizes the light-curves of SNe Ia.

In addition, Figure 2 shows the true sample size available to each model at each phase t relative to maximum light. This accounts for the specifications given in the previous paragraph, including SNe Ia whose spectra may be interpolated or otherwise are within -5 to $+10$ days of t . Accordingly, the sample sizes available for our models at early times are typically around 20–30 SNe Ia, peaking at 34 SNe Ia available when attempting to do an extrapolation of a spectrum taken around $t = +0$ days. This is still a low sample size, however PCA is chosen for this analysis because it tends to work well with low sample sizes due to its simplicity.

Fortunately, the optical and NIR data sets have good combined wavelength coverage. This allows for two spectra chosen from the two data sets to be merged into a continuous spectrum of a SN Ia representing time t that spans the optical and NIR. Nearly all optical and NIR spectra have shared wavelength coverage between 0.81 – $0.84 \mu\text{m}$. Choosing the higher value of this range to remove optical fringing in the NIR data, we choose to scale the NIR spectrum by a constant factor that allows the two spectra to be equal at $0.84 \mu\text{m}$. As the optical and NIR spectra are separately smoothed prior to merging, described in more detail in § 3.1, noise around $0.84 \mu\text{m}$ should not affect this scaling factor much. The

two spectra are then merged into a full optical+NIR spectrum for that SN Ia, ignoring everything redward of $0.84 \mu\text{m}$ for the optical spectrum and blueward of $0.84 \mu\text{m}$ for the NIR spectrum. This entire process is performed for each supernova until a complete sample of spectra representative of each time t that span both the optical and NIR is achieved.

As stated in § 2.1, the individual optical and NIR spectra are unable to be consistently color-corrected. Consequently, each final merged spectrum is also not corrected to match the photometric colors. We discuss potential impacts of this on the results in more detail in § 5.3.

3. METHODS

3.1. PCA Method

PCA is a dimensionality-reduction technique that allows one to describe the variation in a sample of training data made up of N vectors of the same dimension. In this case, the sample here is a set of compiled spectra described in § 2.2. To transform each spectrum into a vector in the same space, each spectrum in the training sample is interpolated to the same points in wavelength space. This interpolation is performed via a Gaussian process regression using Spextractor (see Burrow et al. 2020, for a more in-depth discussion of this process). As a result, the spectra are also smoothed, eliminating much of the noise each spectrum may contain.

To account for any spectra in the sample that have relatively high flux uncertainty, for example in telluric regions, a variant of standard PCA called expectation-maximization PCA (EMPCA) (Roweis 1997; Bailey 2012) is used. EMPCA uses estimates of uncertainty of input data to weight each sample such that the variation described by eigenvectors is not dominated by high-noise samples or extreme outliers. It is also particularly useful when working with data sets with missing points.

Typically one weights each point by a quantity similar to the inverse variance $1/\sigma^2$; however, in our testing we found this particular weighting scheme leads to noisy eigenvectors, possibly due to the fluctuation in the errors from point to point on the spectra. This does not significantly affect the end results when reconstructing spectra with more eigenvectors (discussed in § 3.3), however when attempting to reconstruct spectra with fewer eigenvectors, the predictions become much noisier. We instead make use of a weighting scheme that is linear in variance, such that the weight of the i th wavelength point of each sample is given by $1 - 0.75 \sigma_i^2 / \sigma_{i,max}^2$, where $\sigma_{i,max}^2$ is the largest variance exhibited at that wavelength across all samples. The factor of 0.75 is inserted to prevent high-variance data from being given zero weight, and it is an arbitrary parameter that de-

scribes the relative weighting between high- and low-variance data points. This min-max scaling of flux variance chosen for the weighting scheme is not standard, but we find it works well in limiting the weight of spectra containing relatively high uncertainties.

3.2. PC Training

Once the sample spectra are interpolated in wavelength space (as discussed in § 3.1), applying PCA will effectively be looking at how each individual wavelength point varies for each spectrum in the sample, and connecting them to form spectrum-like eigenvectors. Because of this, we may choose any set of wavelength points for our training data. However, to be consistent and eliminate as many variables from this analysis as possible, we choose to use spectra only in the range of 0.50–2.30 μm . We typically do not use data blueward of this region because we find in testing that including Fe-group features blueward of 0.50 μm adds too much variation to the training sample given the available sample sizes, leading to lower quality fits and less consistent predicted results. This variation stems from sources such as line blanketing and Ni mixing (see, e.g., Baron et al. 2006; Hoeflich 2017; DerKacy et al. 2020). The exact reason that adding more information to the model blueward of 0.50 μm leads to inferior results is unknown. However, this seems to suggest that the features in this bluer optical region are not correlated with much of the NIR in a way that PCA can describe easily with the limited data available. Perhaps studying the variation in the UV+optical region is the subject of future work when more data is available, but with our current data limitations it is outside the scope of this project.

Once a set of spectra that represent the same time and the same points in wavelength space is compiled, they need to be normalized and standardized before performing PCA. First, each spectrum is individually normalized by its mean value of flux between 0.50–0.84 μm . This is chosen because normalizing by the mean (rather than, for example, the maximum flux value) eliminates some of the variation between spectra due to intrinsic differences in color or other related quantities. It is important to note that PCA is quite dependent on the choice of normalization used, so another normalization may produce different results.

After this normalization, the training data are all uniformly standardized. This includes subtracting the total mean spectrum μ_F of all spectra in the sample, and subsequently dividing them by the standard deviation of the sample, σ_F , such that the variation of flux in the sample at each wavelength point has a standard deviation of 1. This ensures that the eigenvectors are describing

true variation from the mean, and that each wavelength point is on the same scale. This is important because there would be a larger magnitude of variation in the optical part of a spectrum than the NIR region, as spectra typically exhibit higher values of optical flux.

3.3. Prediction Using PCA Eigenvectors

EMPCA produces a basis of eigenvectors that describe most of the variation in the training data sample. It is desirable for these eigenvectors to capture either physical or non-physical correlations between different regions in wavelength space. As an example, the third PC may describe that the sample typically exhibits increased O I and NIR Ca II simultaneously, which would hint that the two features may be correlated to some extent for SNe Ia. Indeed this is the case for spectra at maximum light, as shown in § 4.1. A more in-depth discussion of the behavior of eigenvectors for maximum-light spectra is also given in § 4.1.

By making use of these correlations or anti-correlations, if the spectroscopic behavior of a SNe Ia can be predicted in the NIR using an observed optical spectrum, the optical spectrum can be projected onto the optical part of each eigenvector in the basis to get a set of eigenvalues. This projection is done via a simple dot product, treating the spectrum and eigenvectors as vectors in wavelength space. It should be noted that the spectrum first needs to be normalized and standardized in the exact same manner as the training data (discussed in § 3.1). The resulting projection values just correspond to the eigenvalues needed to reconstruct the optical part of the spectrum — which is already known — using the eigenvector basis. In other words, these projection values describe the extent that each eigenvector describes the optical spectrum. To extrapolate the spectrum in the NIR region, the optical eigenvalues may then be used with the full eigenvectors that span both the optical and NIR regions to form a linear combination that reconstructs the spectrum in both the optical and NIR. This is possible because each eigenvector individually describes both optical and NIR variation simultaneously. Because the data have been standardized, the variation seen in the optical and NIR will be on the same unit-scale. This process may also be performed with any subset of the eigenvector basis, but we assume that the reconstruction is more precise with more PCs used, as each PC accounts for further variation in the sample. However, higher-degree PCs could be capturing pure noise and are therefore often irrelevant to much of the analysis and the prediction.

3.4. Uncertainty Measurement

A measurement of uncertainty for these predictions is given by accounting for two different sources of variation. The first of which comes from uncertainty in how well the eigenvectors are able to be used to make the exact same predictions for the training sample itself, including the same region projected onto the eigenvectors to make a prediction. More specifically, the same prediction is made for each SN Ia in the training sample, and then the sample standard deviation of these predictions is used as part of the total uncertainty. This treats each wavelength point as purely uncorrelated, that is, the noise is treated as white noise. However, the wavelength points in the spectrum are correlated by the underlying physics. In a future release of our code, we will correct for this correlation, but it is beyond the scope of the present work.

Secondly, if there is uncertainty in the flux in the known part of the spectrum that is being extrapolated, this could affect the prediction and therefore must be represented in the total uncertainty. To account for this, we assume that the flux uncertainty is distributed normally and draw 500 samples of the spectrum. Using these samples we then make the same predictions using the same projection and prediction regions, and the standard deviation in these predictions is calculated. This is then added in quadrature to the previous source of uncertainty to make up the total uncertainty in the reconstructed spectrum.

4. RESULTS

4.1. *Maximum-Light Eigenvectors*

When a standardized training data set has been established to represent some point in time, a model may be created that includes a set of N eigenvectors which describe the N highest degrees of variation around the mean of that sample of spectra. [Figure 3](#) shows the first four eigenvector spectra that describe the highest amount of variance in the training sample of 33 unique SNe Ia spectra observed at or around maximum light ($t = 0$) given by the EMPCA algorithm. Note again that these eigenvectors are standardized, showing unit-scaled variation around the mean spectrum μ_F .

In [Figure 3](#), it can be seen that the first PC seems to represent a broad correction to spectra. This could be related to some stretch- or color-like quantity; however, this is unclear as later in [§ 5.2](#) it can be seen that the first PC is not exactly correlated with the color-stretch quantity s_{BV} , but rather a linear combination of PCs may describe s_{BV} . The other PCs seem to describe more individual feature behavior. The typical location of some of the major SN Ia spectroscopic features are indicated and colored in [Figure 3](#). Because of the abstract

nature of these eigenvectors, it is unclear visually if an individual PC captures all information about individual features. For example, both the third and fourth PCs seem to explain variation around Si II $\lambda 6355$, although one may be explaining its depth or pseudo-equivalent width while the other makes corrections in accordance with the Si II $\lambda 6355$ velocity extent. This is discussed in a more quantitative manner in [§ 5.1](#).

The cumulative fraction of explained variance for each subsequent eigenvector is shown in [Figure 4](#). As may be seen, 10 eigenvectors explain up to 94.8% total variation of the training sample. Because the spectra have been standardized at all wavelengths, this demonstrates that 10 eigenvectors is sufficient in reconstructing typical spectra belonging to the same population of SNe Ia.

We speculate that much of the variance that is unexplained by the PCs may stem from the relatively high uncertainty in the corrections to NIR telluric regions made for the FIRE data set. In the near future, the negative impact of telluric features on data driven models may be mitigated with JWST observations of SNe Ia (see, e.g., [Kwok et al. 2023](#)).

4.2. *Prediction Near Maximum Light*

Unfortunately, there is much complexity in the time- and wavelength-dependence of these predictions. There are also not many homogeneously observed spectra available in both the optical and NIR at nearby phases in time outside the sample used in the PCA here. Because of this, a formal test and quantitative statistical analysis of how well this method actually performs is difficult to achieve. Instead, to illustrate the potential of this method, in this section we show a few near-maximum-light examples of this extrapolation procedure. In particular, we show this in [Figure 5](#) for SNe 2011fe, 2021fxy, 2021aefx, and 2022hrs, which are a few diverse, well-observed SNe Ia that are all outside the training sample used to create the maximum-light eigenvectors shown in [Figure 3](#) and discussed in [§ 4.1](#). Because the full optical–NIR range of these SNe Ia is required here for comparisons, the closest optical and NIR observations to maximum light available to us were merged into the black line shown in [Figure 5](#). It should be noted that some of these NIR spectra were observed days apart from their optical counterparts, which may affect results, though this is not avoidable due to data limitations.

Each of the panels of [Figure 5](#) show a prediction for 0.50–2.30 μm indicated in red. They are compared with their respective rest-frame observed spectrum in black, part of which was used to generate a prediction. These observations are referenced and further elaborated on below. Vertical dashed lines indicate the 0.50–0.84 μm

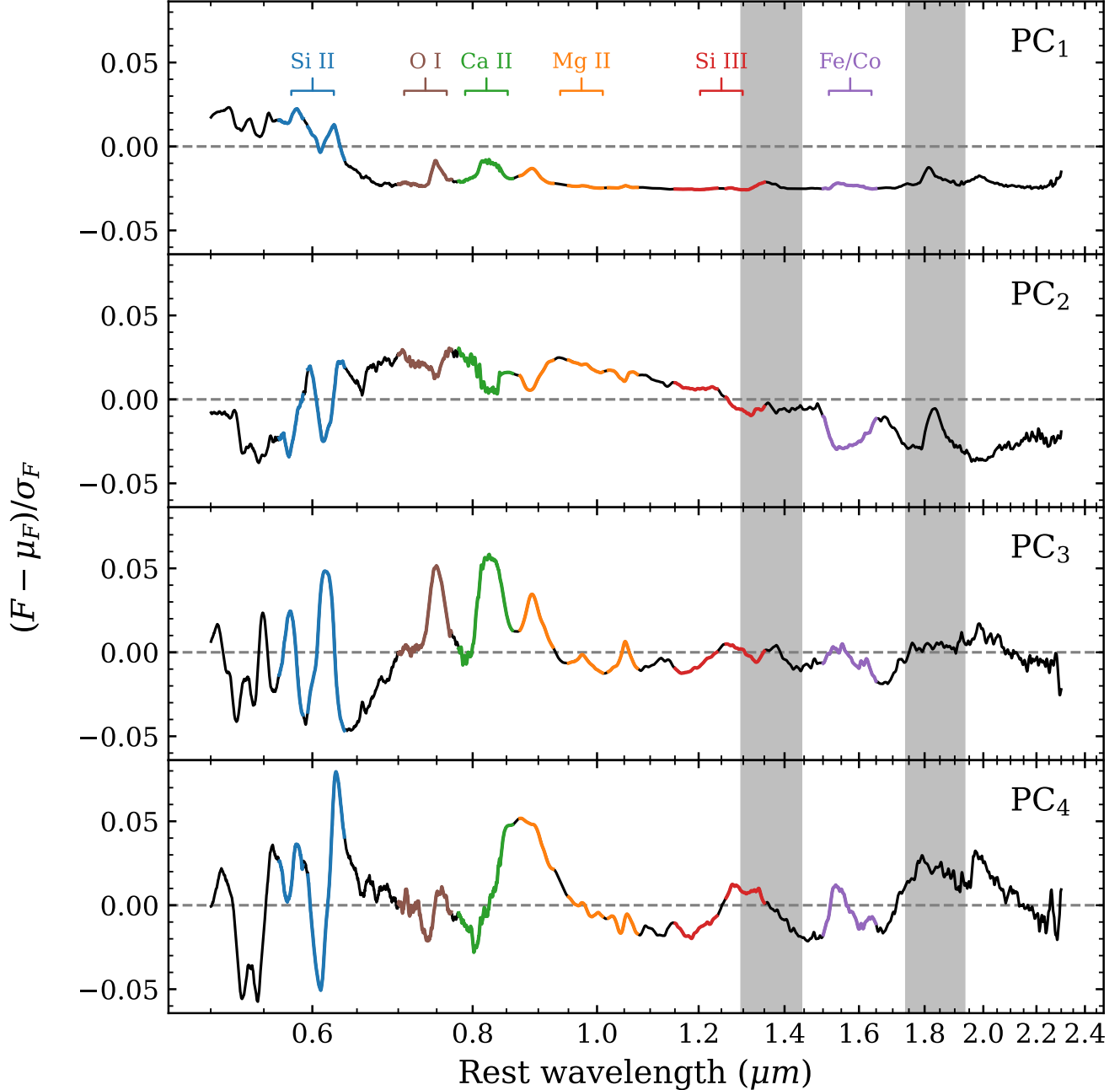


Figure 3. The first four PC eigenvectors representing $t = 0$ that describe the highest degrees of variation in the near-maximum-light standardized training data set. These vectors lie within wavelength space, and note that these eigenvectors represent unit-scaled variation from the mean spectrum. Grey shaded regions indicate the larger telluric regions in the NIR.

region that is projected onto the PC eigenvectors to make this prediction. A measurement of uncertainty for the prediction (see § 3.4) is shown in the light red shaded area. The two NIR telluric regions between 1.2963–1.4419 μm and 1.7421–1.9322 μm are shaded in gray. Percent-differences between the PCA reconstructions and observed spectra are shown below each spec-

trum; note that these differences are in flux space — not in log-flux space.

The top-left panel of Figure 5 shows the extrapolation of a near-maximum spectrum of SN 2011fe (Mazzali et al. 2014). Calculating Si II line velocity $v_{\text{Si II}}$, $\text{pEW}(\text{Si II } \lambda 6355)$, and $\text{pEW}(\text{Si II } \lambda 5972)$ using this spectrum, and using values with Gaussian mixture models (GMMs) from Burrow et al. (2020), SN 2011fe is

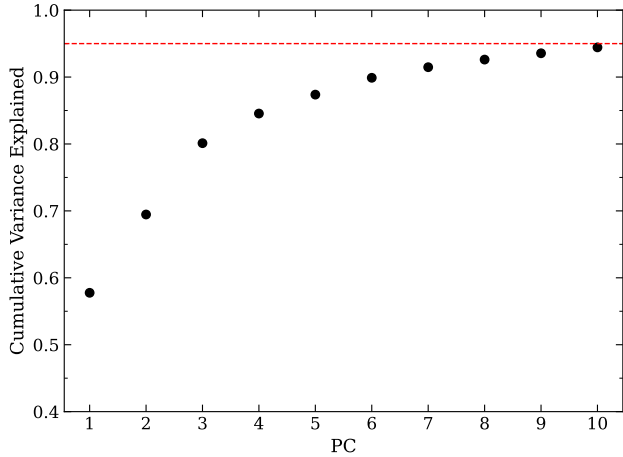


Figure 4. Cumulative fractional variance of the training spectra explained by the eigenvectors in Figure 3. The red dashed line represents when a total of 95% explained variance is achieved.

classified to be a CN SN Ia with a probability of 74.2%. Because SN 2011fe has historically been so well-observed and studied, this SN Ia is included here to illustrate our extrapolation performance on a quintessential test case using this spectroscopically normal SN Ia.

Looking at the prediction for SN 2011fe in Figure 5, the reconstruction of the spectrum performs well within the region projected onto the eigenvectors (indicated by dashed lines), and the uncertainty is relatively small. There is at most a nearly 35% difference in the flux of observation and prediction in this region where the depth of Si II $\lambda 6355$ is not fully reproduced. Outside this region — past $0.84 \mu\text{m}$ where the extrapolation actually occurs — the general trend of flux is captured by the prediction, as well as most individual feature behaviors outside the two large telluric regions in the NIR. However, in this region the uncertainties are much larger. In addition, at around $1.5 \mu\text{m}$ the prediction begins to deviate from the observations. Between $0.9\text{--}1.5 \mu\text{m}$, the median percent-difference in the flux is -10.5% — not including flux in telluric regions, which will continue to be ignored for other median values provided. After $1.5 \mu\text{m}$ the same median jumps to $+18.8\%$ difference in the flux. Although these figures seem high, when integrating the quantity λF_λ across the extrapolated spectrum between $0.84\text{--}2.30 \mu\text{m}$, ignoring telluric regions in this integral, the difference is only -3.1% . This difference in the integral gives perhaps a better figure of merit when making corrections to photometry than looking at only the median percent-difference in the flux.

In the top-right panel of Figure 5, a near-max spectrum of SN 2021fxy (DerKacy et al. 2023) is shown alongside its NIR prediction. The observation is, similar

to the SN 2011fe spectrum from (Mazzali et al. 2014), a merge of an optical spectrum around $+0$ days and a NIR one around $+1$ days. This process of merging normalizes the NIR spectrum to the optical spectrum by the integrated flux within $0.84\text{--}0.88 \mu\text{m}$, and performs a weighted average to get the new merged flux for that region. SN 2021fxy was determined by GMMs to be a SS SN Ia with a probability of 95.5%. The prediction here is quite similar to that of SN 2011fe, however all merits of fit discussed for SN 2011fe were more true to the observation for SN 2021fxy, even with a noisier spectrum, aside from a poorer fit to NIR Ca II around $0.8 \mu\text{m}$. In the $0.9\text{--}1.5 \mu\text{m}$ region, the median difference in flux was -5.6% , and past $1.5 \mu\text{m}$ the median is $+4.0\%$. Integrating the observed and the predicted spectra in the same way as before shows a difference of -2.9% . It seems that although the eigenvectors shown in Figure 3 appear to show substantial variation of Si II features, shallower Si II lines that are projected onto these eigenvectors do not lead to a less accurate prediction.

The bottom-left panel of Figure 5 shows a near-maximum spectrum of SN 2021aefx (Burns et al. 2021; Hosseinzadeh et al. 2022) as well as its extrapolation. The observed spectrum is merged in the same way as SN 2021fxy with an optical spectrum at $+3$ days and a NIR spectrum at -1 days. SN 2021aefx is classified with GMMs as a CN with a probability of only 57.6% and therefore may exhibit some atypical spectroscopic behavior relative to most CN SNe Ia. Within $0.50\text{--}0.84 \mu\text{m}$, the fit to the observation including Si II is good except for the noisier region around $0.80 \mu\text{m}$ where there is more fringing of the original optical spectrum. As such, the fit to NIR Ca II is poor. Still, the NIR prediction of this spectrum performs reasonably, with a median percent difference in flux of $+7.8\%$ until $1.5 \mu\text{m}$ where this difference increases, reaching a median of -13.6% . SN 2021aefx continues to compare well to the observation with a difference in integrated flux of -2.7% .

Finally, the bottom-right panel of Figure 5 shows a 100%-likely BL SN Ia (rounded up from a GMM calculation of 99.98% probability), SN 2022hrs (Burns et al. 2021, P. Brown et al., in prep.). The observation shown here is made from merging an optical spectrum at -1 days and a NIR spectrum at $+6$ days. This SN Ia provides an interesting outlook as no BL SNe Ia exist in the maximum-light training data set used to make this prediction. This possibly explains the relatively poor fit to the observation in the $0.50\text{--}0.84 \mu\text{m}$ region, and especially when reproducing Si II $\lambda 6355$. It seems that a linear combination of PCs that is able to describe the depth of Si II $\lambda 6355$ alongside other features not ob-

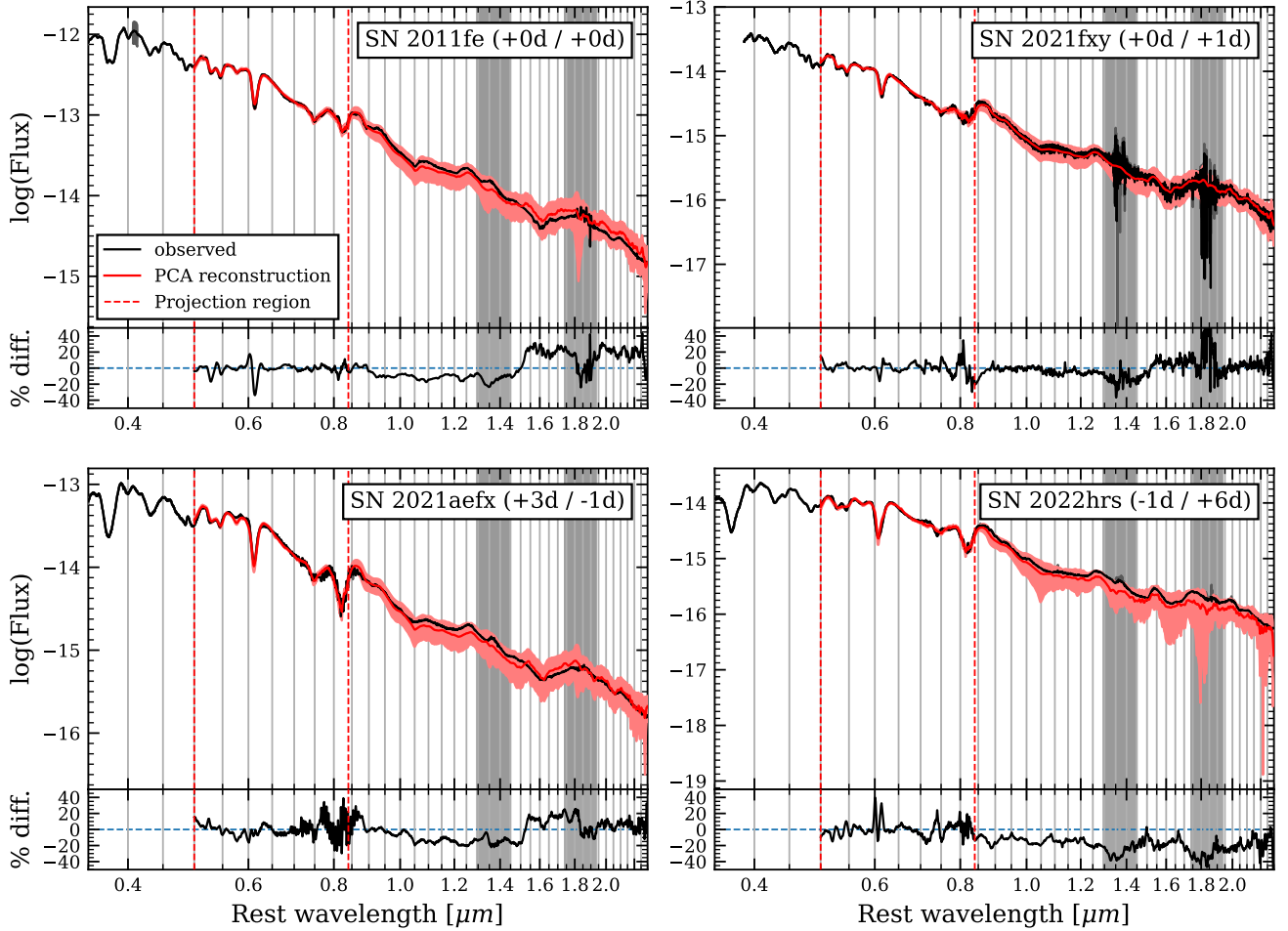


Figure 5. The extrapolation of different SNe Ia near maximum light shown in red, compared with the true observed spectrum in black. Uncertainties in the predictions are given by the red shaded areas. Grey shaded areas specify telluric regions in the NIR. The region between red dashed lines is projected onto the maximum-light eigenvectors to make this prediction. Percent-difference between the prediction and flux is given on the bottom of each panel; note this difference is not calculated from log-space. Phases shown are the phases of the optical and NIR spectra, respectively, that were merged to create the observed spectrum.

tainable without more BL data included in the training sample. There are also larger uncertainties involved with this spectrum. The most glaring difference between this SNe Ia and the other three examples is that there seems to be a $\sim 20\%$ near-constant negative offset between the prediction and observation after $0.84 \mu\text{m}$. This again may be due to the eigenvector training sample not including BL SNe Ia, and therefore a BL such as SN 2022hrs is not represented well enough to accurately reconstruct its spectrum in either the optical or the NIR. In fact, we see this later in § 5.3 with SN 2014J, a CN SNe Ia with high $v_{\text{Si II}}$, similar to BLs. This offset may also be due to the seven-day difference in observation time between the optical and NIR spectrum used

to create the observation shown. With this offset seen for SN 2022hrs, the difference in integrated flux between the prediction and observation is -17.7% , substantially greater than the other three example SNe Ia.

Although Figure 5 demonstrates a good comparison between predictions and their respective observed spectra, it is difficult to determine any significant difference between the predictions, and whether or not the characteristic differences between SNe Ia subtypes are being represented well by the predictions. For this reason, we also provide a direct comparison of the predictions themselves in Figure 6. The left panel shows the observed spectra from each SNe Ia in Figure 5 past $0.84 \mu\text{m}$. The spectrum in the telluric regions of SN 2021fxy was omit-

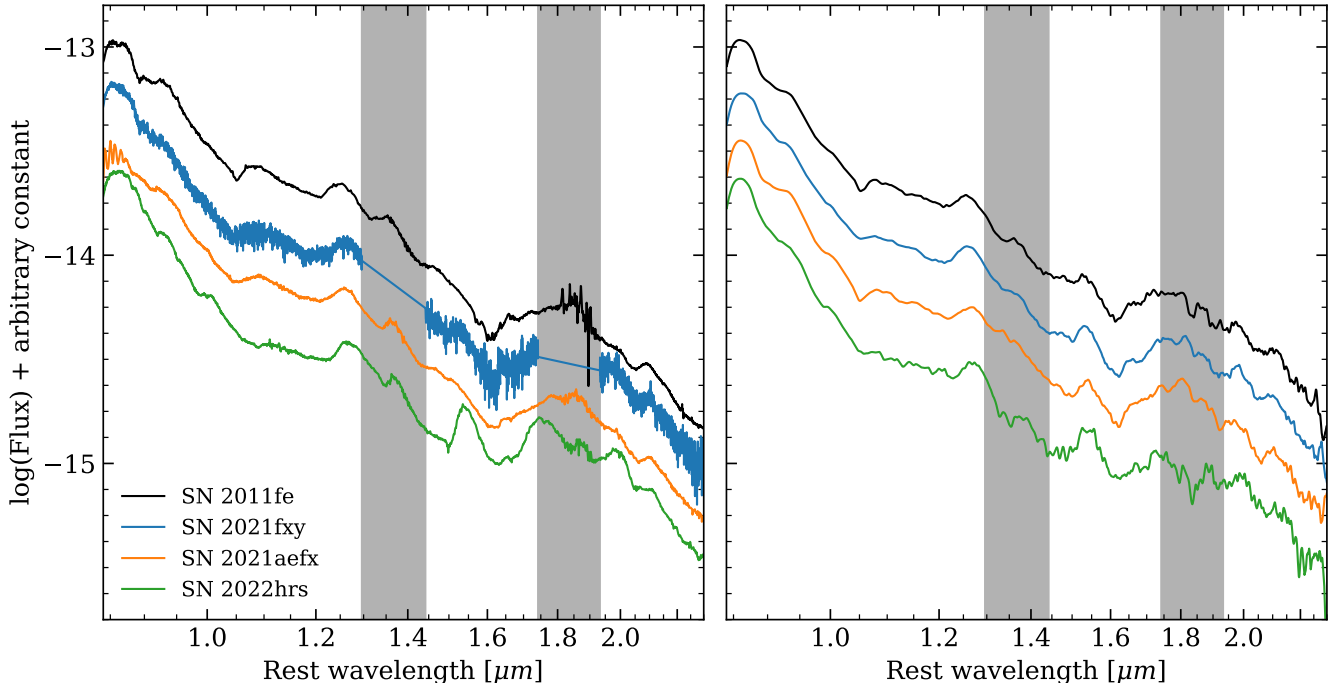


Figure 6. A direct comparison of the four near-maximum-light observations from Figure 5 (left panel) and their corresponding extrapolations (right panel) in the NIR. The extrapolations appear to capture many of the distinctions shown between the observed spectra, except for the Fe II feature near $1.50 \mu\text{m}$.

ted for visual clarity due to the high amount of noise. In the right panel, the corresponding predictions (red lines from Figure 5) are plotted. Each spectrum was normalized by the integrated flux of the $0.84\text{--}2.30 \mu\text{m}$ region, ignoring the telluric regions in the grey shaded region, with SN 2011fe as the reference. The spectra are then equally spaced from each other in the figure.

Here it is beneficial to summarize the Branch groups to which each SN Ia here belongs: SN 2011fe and SN 2021aefx are classified CNs, SN 2021fxy is a SS, and SN 2022hrs is a BL SN Ia. Keeping this in mind, the predictions seem to do very well at the feature level in capturing the differences between these SNe Ia. Using line identifications by Hsiao et al. (2019), Mg II around $0.92 \mu\text{m}$, $1.09 \mu\text{m}$ is conserved in the prediction, being stronger for the CNs, slightly weaker for the SS, and weakest for the BL SN Ia. However, the predicted Mg II at $1.09 \mu\text{m}$ appears much more narrow than the observation for SN 2021aefx. Mg II near $2.10 \mu\text{m}$ appears strong for the BL SN Ia as well, and the prediction captures the observations well for this feature, including the feature shape. Si III near $1.25 \mu\text{m}$ is similar for each SN Ia in both the observation and the prediction. Using line identifications displayed by Friesen et al. (2014), the Co II feature around $1.65 \mu\text{m}$ is also differentiated well in the prediction for each subtype, including the feature shape. The biggest departure from the obser-

vation that the prediction contains is the Fe II feature around $1.50 \mu\text{m}$. Fe II here is much more shallow for CNs, which is not expressed by the predictions. In general, though, the feature behavior between SNe Ia of different Branch groups appears to be captured well by these predictions.

4.3. Time-Dependent Predictions

We showed in § 4.2 that the extrapolation process performs fairly well for spectroscopically normal SNe Ia near maximum light. However, when extrapolating at other phases, the results and performance of this technique may lead to less certain predictions, especially due to decreasing training sample sizes. As expected from the sample sizes given in Figure 2, at later times the available number of training spectra decreases significantly as there are not as many concurrent optical and NIR observations in the CSP I+II data set. Interpolation at these later times is often not possible, as either the total number of observations of each individual SN Ia are too few, or the observations were too far apart in time to give reasonable interpolations. However, up to around 20 days past maximum light, the available sample size is still around 20 SNe Ia—twice the number of eigenvectors we use to model spectra, which may generate reasonable extrapolations of spectra observed at these phases.

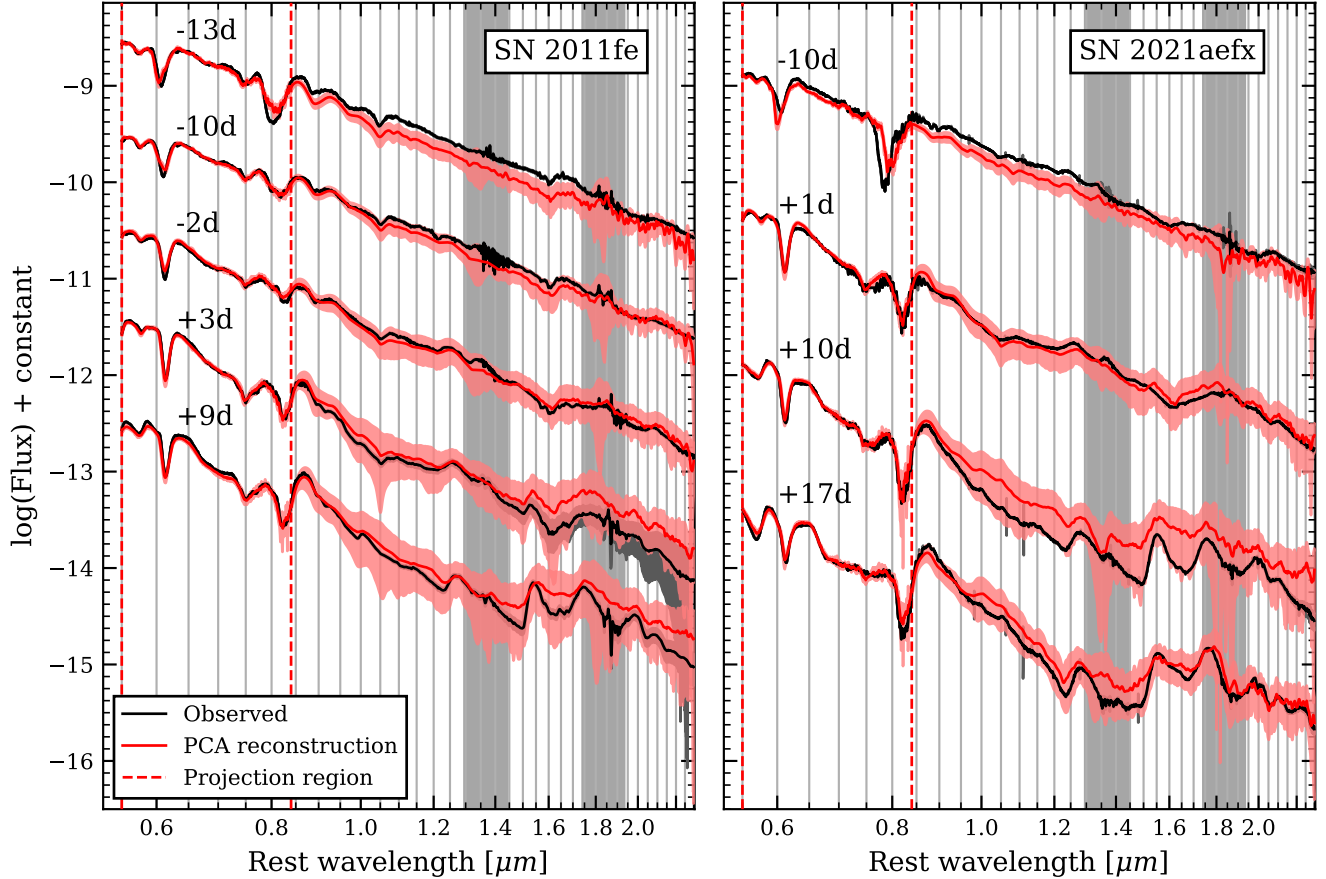


Figure 7. Extrapolation for a time series of SN 2011fe and SN 2021aefx. All formatting and notation is the same as in Figure 5.

In Figure 7 we show the same prediction process as in § 4.2 on a time series of early spectra of SN 2011fe (Mazzei et al. 2014) and SN 2021aefx (Burns et al. 2021; Hosseinzadeh et al. 2022), as they have good concurrent observations in both the optical and NIR surrounding maximum light. Both SNe Ia yield similar results. At earlier times, most feature behavior is captured, aside from Ca II around $0.80 \mu\text{m}$. The prediction for SN 2011fe also introduces a small constant offset from the prediction across the NIR that is not exhibited by SN 2021aefx. This may be due to differences in the flux calibrations between the optical and NIR spectra, which cannot be corrected for in the merging process due to a lack of photometric data for the entire data set (see § 5.3).

At later times, the general trends of the flux of both SNe Ia are captured; however, much of the feature information beyond $1.5 \mu\text{m}$ appears to be lost, and the uncertainties are much larger. This could mean that there is more variation in this region than can be explained with the limited sample size available.

4.4. Prediction Using Si II

For consistency we used the $0.50\text{--}0.84 \mu\text{m}$ region to project onto the eigenvector basis in order to make predictions. However, this region itself is a variable and may be changed. Increasing this range is impractical as, again, using information blueward of $0.50 \mu\text{m}$ introduces much of the UV-optical variation that is difficult to explain using a limited training sample. Instead, this section focuses on the outcome of narrowing this region to a more meaningful one.

It is clear that the Si II $\lambda 6355$ and Si II $\lambda 5972$ features in the optical are important observables in the diversity of SNe Ia, as they make up the basis of the Branch classification system, which has been shown to yield a statistically significant set of groups with distinct characteristics (Burrow et al. 2020). Figure 8 shows the result of projecting only the $0.55\text{--}0.64 \mu\text{m}$ region consisting of these two Si II lines onto the eigenvector basis to extrapolate into the NIR up to $2.3 \mu\text{m}$. This was done for the same SNe Ia as in § 4.2, and the figures show the same information as shown in Figure 5; the only change is the region used to make the prediction, shown as red dashed lines. It is important to reiterate that the

only information provided to the maximum-light model is this narrow Si II window — aside from the mean flux value of the 0.50-0.84 μm region required to normalize the spectrum in the same way as the training data.

The predictions shown in Figure 8 are quite surprising, given the small amount of information provided. Comparing SN 2011fe and SN 2021fxy in Figure 5 and Figure 8, the predictions are quite similar. For each SN Ia, both cases seem to predict the general flux behavior of the observation fairly well. The uncertainties shown are nearly the same across each spectrum between the two cases, except they are much improved in the case of SN 2022hrs where spikes of larger uncertainties are shown at some wavelengths past 1.5 μm . The most notable difference between these two cases is the inability to reproduce the NIR Ca II triplet well. This seems to suggest that Ca II behavior is not strongly dependent on Si II $\lambda 6355$ and Si II $\lambda 5972$ near maximum light.

The integrated flux differences from the observations in this case are -2.4% for SN 2011fe, $+2.0\%$ for SN 2021fxy, -0.4% for SN 2021aefx, and -18.5% for SN 2022hrs. This means that the prediction was marginally improved for SN 2011fe, SN 2021fxy, and SN 2021aefx, and only weakened for SN 2022hrs, which is likely because it is a BL, unlike the SNe Ia in the training set. Given just these few test spectra shown here, no conclusion is drawn regarding which case performs better. However, the similarity in results between the two cases indicates that Si II may be the only requirement for a reasonable prediction in the NIR in general.

5. DISCUSSION

5.1. PC Relation to Branch Groups

Because the NIR spectrum seems well-inferred by projecting only the two Si II features onto the eigenvectors, one may think that the eigenvectors themselves have some relation to the Branch group classification scheme. Here we look at how these eigenvectors relate to the Branch groups to explore the possibility that each individual Branch group has unique spectroscopic features that exhibit a relationship with features in the NIR.

We project 101 near-maximum-light spectra (within ± 5 days of maximum light) available from the optical CSP I & II data set onto the maximum-light eigenvectors shown in Figure 3. However, we only project the region between 0.55–0.66 μm in order to account for the extent of Si II $\lambda 6355$ and Si II $\lambda 5972$ on the eigenvectors. These values — denoted as PC₁, PC₂, etc., corresponding to the projection onto the respective eigenvectors — are then plotted against each other in the correlation matrix shown in Figure 9. The pEWs of Si II $\lambda 6355$ and

Si II $\lambda 5972$ as well as Si II $\lambda 6355$ expansion velocity $v_{\text{Si II}}$ of each spectrum were calculated using Spextractor. By using a 3-D Gaussian mixture model from Burrow et al. (2020), the Branch group that each SN Ia is assigned to lie within has been colored in a similar fashion to Burrow et al. (2020). In addition, SNe Ia exhibiting higher velocities with $v_{\text{Si II}} > 12,500 \text{ km s}^{-1}$ are symbolized with stars in Figure 9. Many of these high-velocity (HV) SNe Ia are classified as CNs or BLs, which is seen in Burrow et al. (2020).

It is immediately apparent that a few subspaces, for example PC₁ vs. PC₃ or PC₂ vs. PC₄, seem to show CN, SS, and CL SNe Ia lying in distinct regions, similar to a classic Branch diagram. There are some exceptions to this, for example in the PC₁ vs. PC₃ panel, several CNs lie in the region dominated by SS SNe Ia. This illustrates that there is not a one-to-one relationship between these projections and the measured pEWs of Si II $\lambda 6355$ and Si II $\lambda 5972$, and therefore this is not a recreation or rotation of the classic Branch diagram. This is further explored in the discussion of Table 1 later in this subsection. This suggests that there may be some intrinsic differences between these CNs lying within the SS-dominated region in this subspace and the other more concentrated CNs. Many of these CNs within the SS region exhibit higher velocities; however, this likely cannot be the only characteristic that sets these SNe Ia apart from other CNs, because other HV CNs are seen in the concentrated region as well. Finally, note that BL SNe Ia are not as constrained to their own regions in Figure 9. This could be due to the unfortunate lack of BL representation in the training sample used to calculate these eigenvectors. Because of this, it is difficult to arrive at concrete conclusions for BL SNe Ia from this figure.

Investigating the PC_{*i*} subspaces further, Figure 10 plots the projections of Si II onto PCs 2, 3, and 6 against pEW(Si II $\lambda 5972$), pEW(Si II $\lambda 6355$), and $v_{\text{Si II}}$, respectively. Each point is colored by Branch group classification in the same way as Figure 9. Linear regression lines are shown for each panel; the red line shows the regression for all points, and the blue line shows the same for all points except high-velocity SNe Ia. The R^2 coefficient of determination for each regression line is shown in the legend of each panel. A summary of the R^2 values for each projection up to PC₈ against all three spectroscopic properties is given in Table 1, where R^2 values from fits excluding HV SNe Ia are given in parentheses. PCs 2, 3, and 6 were chosen to be displayed because they exhibit the highest R^2 for correlations with the three properties for both the general and non-HV cases. Although a low value of R^2 does not rule out a non-

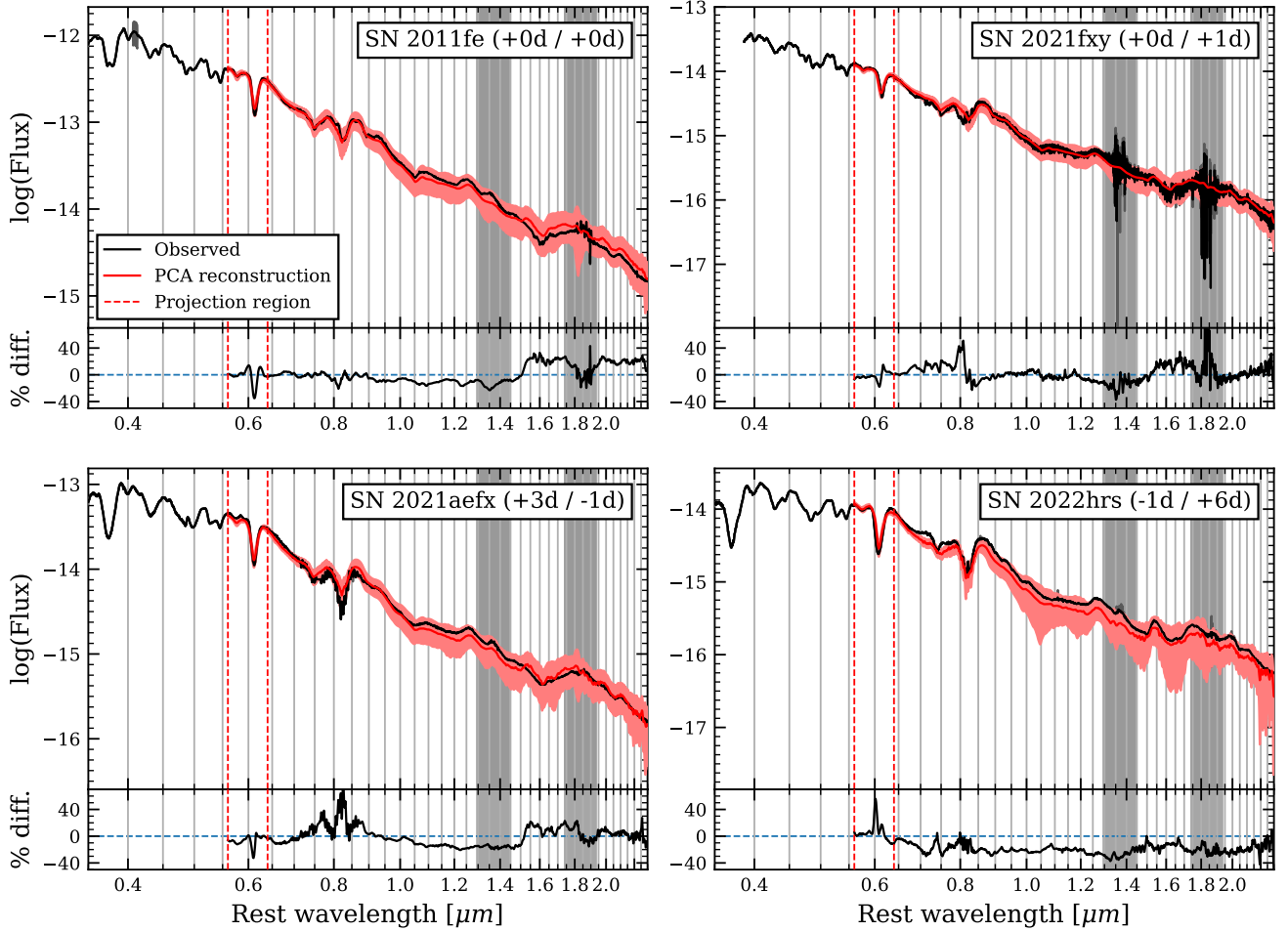


Figure 8. This shows the same spectra as in Figure 5, however the predictions are now made with a narrower optical region dominated mostly by Si II $\lambda 6355$ and Si II $\lambda 5972$. All formatting and notation is the same as in Figure 5.

linear correlation, other values of PC_i are not displayed here because there is no clear visual trend in them, or the spread of the points is too large. This leads to the low values of R^2 for the majority of projections seen in Table 1.

The highlight of this analysis is obtained by observing how PC_3 relates to the $pEW(\text{Si II } \lambda 6355)$ shown in the middle panel of Figure 10. There is a significant spread of SNe Ia around the regression line, however when ignoring the clearly distinct HV SNe Ia in this panel, the spread is greatly reduced, leading to a significantly improved R^2 , which is indicative of a stronger linear correlation between PC_3 and $pEW(\text{Si II } \lambda 6355)$. The effect of HV SNe Ia being outliers from the trend line is also not dependent on Branch group classification — i.e., these outlying points do not only correspond to BL SNe Ia. It appears that the measurement of PC_3

seems to be accounting for HV behavior in a way that the classic measurement of $pEW(\text{Si II } \lambda 6355)$ cannot.

In addition, we find a mild linear correlation between PC_2 and $pEW(\text{Si II } \lambda 5972)$, which itself has been shown to exhibit a connection with s_{BV} (see, e.g., Burrow et al. 2020). However, we show and discuss in § 5.2 that more information than PC_2 is needed to extract an estimate of s_{BV} from a spectrum using these projections. The slope estimator of each linear regression shown in Figure 10 has a two-sided P-value of much less than 0.001, heavily suggesting that there is at least some dependency of these three PC_i and the respective spectroscopic quantities shown. Visually, though, the wide spread of measured PC_2 seems comparable to the change in the trend of PC_2 as $pEW(\text{Si II } \lambda 5972)$ changes and therefore, this linear relationship seems untrustworthy as an estimator. This also seems true for PC_6 versus $v_{\text{Si II}}$, as removing HV SNe Ia in this panel heavily diminishes the quality

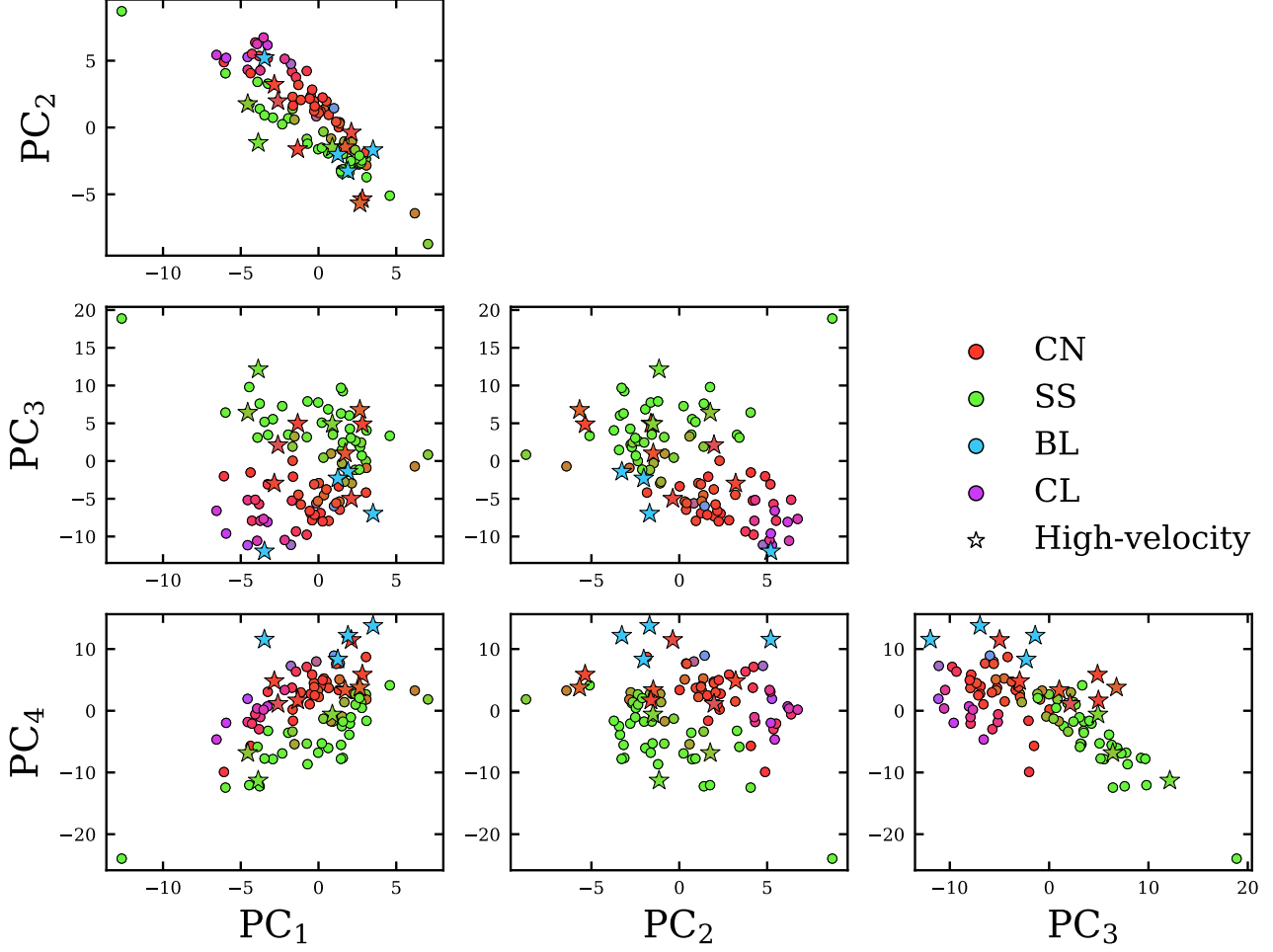


Figure 9. The projections of spectra in the optical data set onto the first four maximum-light PCs in Figure 3 only in the $0.55 \mu\text{m} < \lambda < 0.66 \mu\text{m}$ region. Points are colored for the probability of Branch group classification in the same way as in Burrow et al. (2020) using a 3-D GMM. Points shown as stars are high-velocity SNe Ia exhibiting $v_{\text{Si II}} > 12,500 \text{ km s}^{-1}$ at maximum light.

of this linear correlation, which is suggested by the much lower R^2 statistic.

These projections may offer an alternative method of classifying SNe Ia that does not rely on the assumption of a pseudo-continuum that can lead to inconsistent measurements. It would be interesting to perform further testing with these PC_i measurements to decide their candidacy as classification criteria that may offer solutions to some known discrepancies in SNe Ia classification. For example, Burrow et al. (2020) show that several CNs exhibit high velocities that would be expected of BLs, given the relationship between the velocity of the blueshifted absorption part of a P Cygni profile and its equivalent width. Measuring PC_i values instead of pEWs could reclassify these HV CNs to be similar to SNe Ia with broader Si II $\lambda 6355$ features.

5.2. PC Relation to s_{BV}

Similar to Lu et al. (2023), it is interesting to see how these PCs may be related to light-curve parameterization such as the color-stretch parameter s_{BV} . This relation may play an important role in the connection between observed photometry and the underlying SED of SNe Ia. In Figure 11, the exact same PC projections as those shown in Figure 9 are displayed, now colored for the s_{BV} value of each SN Ia calculated using SNooPy. There appears to be a multi-dimensional trend between s_{BV} and many of the PC values. In other words, by projecting the Si II region of a spectrum onto the maximum-light eigenvectors, this would produce values that should allow one to predict s_{BV} given only spectroscopic information. For example, just using PC_1 and PC_2 , it may be seen that SNe Ia with high values of PC_1 and low values of PC_2 tend to have higher s_{BV} , and vice versa.

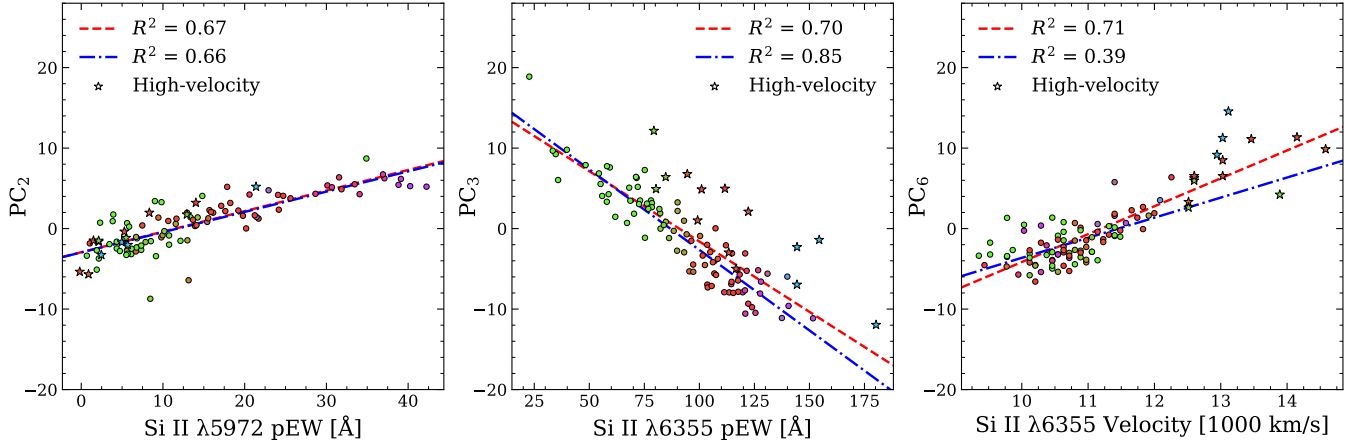


Figure 10. PC_2 , PC_3 , and PC_6 plotted against $pEW(\text{Si II } \lambda 5972)$, $pEW(\text{Si II } \lambda 6355)$, and $v_{\text{Si II}}$, respectively. Colors here are the same 3-D GMM colors shown in Figure 9, and points shown as stars indicate the same HV SNe Ia. Lines here indicate linear regression lines for all the points (in red, dashed) and for all points except HV SNe Ia (in blue, dash-dotted).

Table 1. Summary of R^2 values of all PC_i linear correlations with various spectroscopic properties. Values in parentheses indicate the R^2 value of the linear regression excluding HV SNe Ia.

Projection	R^2		
	[$pEW(\text{Si II } \lambda 5972)$]	[$pEW(\text{Si II } \lambda 6355)$]	[$v_{\text{Si II}}$]
PC_1	0.42 (0.44)	0.02 (0.03)	0.03 (0.06)
PC_2	0.67 (0.66)	0.19 (0.29)	0.03 (0.00)
PC_3	0.34 (0.35)	0.70 (0.85)	0.00 (0.08)
PC_4	0.00 (0.00)	0.49 (0.43)	0.23 (0.35)
PC_5	0.51 (0.51)	0.01 (0.03)	0.42 (0.20)
PC_6	0.04 (0.00)	0.17 (0.06)	0.71 (0.39)
PC_7	0.09 (0.11)	0.61 (0.62)	0.01 (0.05)
PC_8	0.03 (0.03)	0.46 (0.52)	0.02 (0.16)

Looking at the PC_1 column, it appears that PC_1 does not directly correlate with s_{BV} by itself. This is verified by Figure 12, which plots PC_1 against s_{BV} , showing the large amount of spread in the relationship between the two quantities. If one were to use this relationship with a measured value of PC_1 , it would not be possible to estimate an accurate s_{BV} without large uncertainty. This heavily suggests that the first PC shown in Figure 3 does not describe the same variation of SNe Ia within the training sample that s_{BV} explains.

Examining each subplot in Figure 11, the regression of s_{BV} visually appears to define a direction in each subspace, suggesting that s_{BV} may be determined by the projections. This idea of predicting s_{BV} may be put to the test with a simple linear model. This model may be

a function of any number of PC values, i.e.,

$$s_{\text{BV}} = a_0 + \sum_n^N a_n PC_n, \quad (1)$$

where a_n are coefficients for each projection PC_n up to the projection PC_N . After some testing, we find that the sum of least-squares are reduced as more projections are added to this model (and thus N increases). For this example we extend this model up to $N = 8$, and therefore the linear model will contain nine coefficients to be fit. These coefficients are determined by fitting to the data in Figure 11 using least-squares fitting.

To simulate a test of this procedure, we take a random 80% (82 points) of the SNe Ia in Figure 11 to fit the coefficients of the model, then use this model to estimate s_{BV} of the same SNe Ia. These values are displayed in

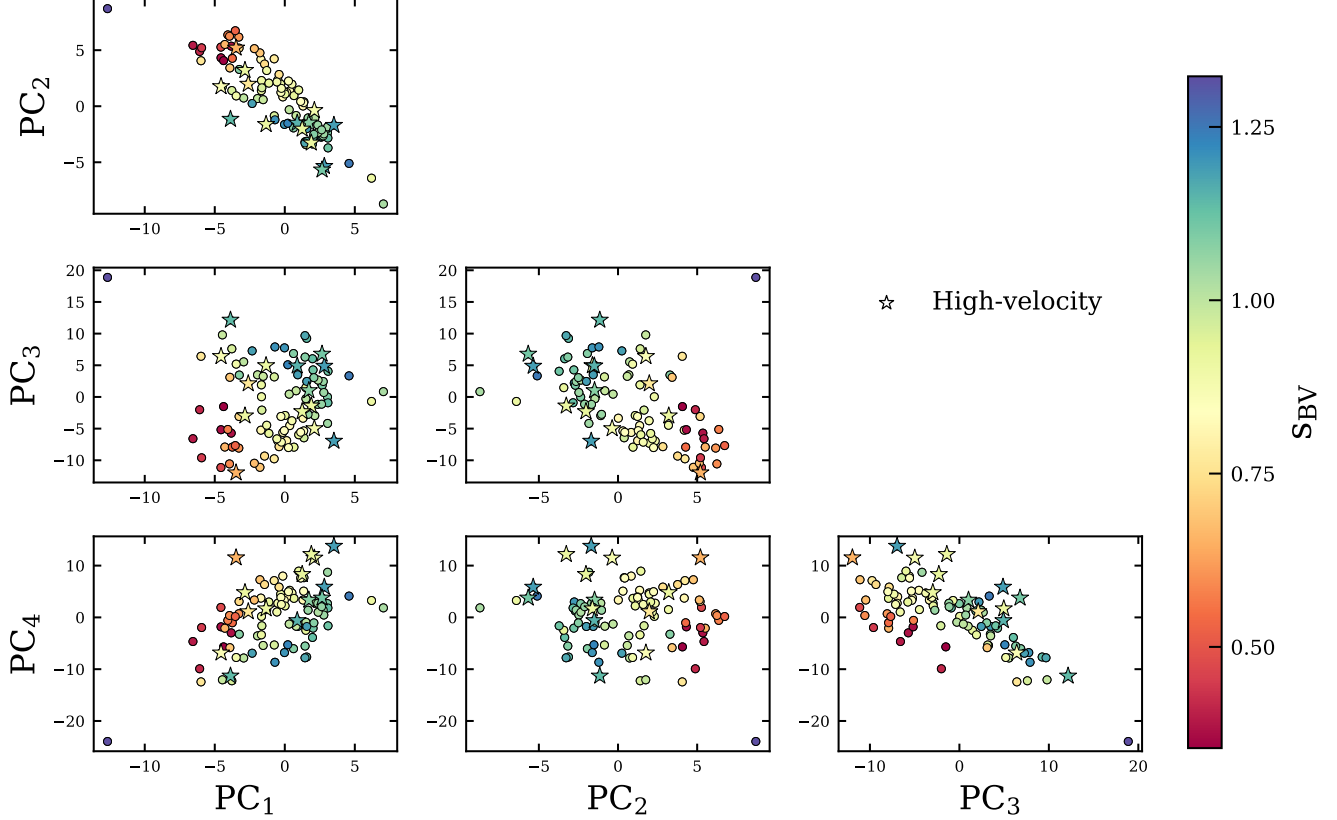


Figure 11. The same projections as in Figure 9, however now colored for s_{BV} determined by SNooPy. It seems visually plausible that s_{BV} may be estimated here as a function of two or more PCs.

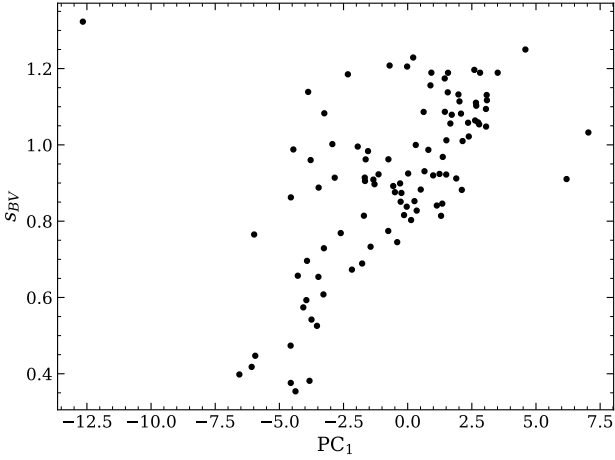


Figure 12. A direct view of PC_1 , from Figure 11, versus s_{BV} . This shows the lack of correlation between the two, showing that more information than PC_1 is needed to estimate s_{BV} .

Figure 13 as black points. The remaining points colored red in Figure 13 are the s_{BV} model estimates of the remaining 19 SNe Ia, from which no information was provided to the model. These s_{BV} values are then

compared with those obtained by the light-curve-fitting tool SNooPy.

We see that the vast majority of these SNe Ia adhere to this model within a spread of about ± 0.1 units of s_{BV} for all values of measured s_{BV} . The testing sample seems to be commensurate with the training sample for all s_{BV} , aside from three outlying test points around $0.7 < s_{BV} < 1.0$, although they do not lie too far outside this trend. In general, for such a simple linear model and method (using of a small region of the spectrum), this fit to s_{BV} values measured with SNooPy is surprisingly good. One could possibly use a more complex regression technique or test other regions in wavelength space to produce better fits (at the risk of over-fitting); however, the purpose of this is to show the simplicity of the correlation of Si II properties with s_{BV} . In addition, for future studies, it could be interesting to see if any outliers to this model exhibit larger residuals in its NIR light-curve as determined by SNooPy. If an observed spectrum yields a substantially different value of s_{BV} for a supernova using these PCs compared to using the observed photometry, this could indicate intrinsic dif-

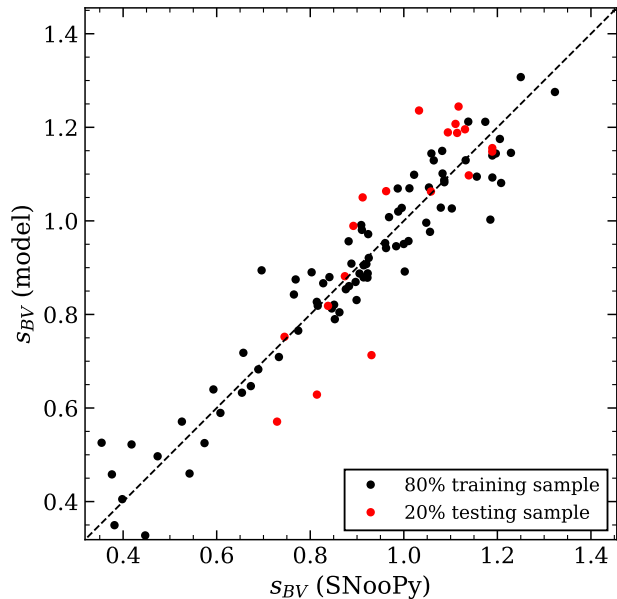


Figure 13. On the x-axis, s_{BV} calculated by SNooPy is shown for the same SNe Ia that produce the points in Figure 11. On the y-axis, s_{BV} is shown, calculated from a linear model described by Equation 1, where the a_n coefficients are determined via a least-squares fit to a random 80% of the available spectra representing black points. The red points are the remaining 20%, illustrating this s_{BV} model fits well with the majority of values given by SNooPy.

ferences in its spectrum which could be seen in its NIR light-curves.

5.3. Color-Matching with Broad-Band Photometry

As discussed in § 2, neither training spectra nor any spectra shown in § 4 have been color-matched to the broad-band photometry. As such, the differences in the flux calibrations between optical and NIR spectra may result in some training spectra having improperly scaled NIR flux. In other words, the photometric color of the predicted spectrum will be incorrect. This may lead to substantial variation in the training data in the NIR. However, if this variation is in any way systematic, the eigenvectors may describe this variation and be able to correct for it, albeit not perfectly. It is not possible to know if this hypothesis is true without observed photometry for all of our training SNe Ia; however, we can still make this assumption. This assumption may be supported by the first PC in Figure 3, which seems to describe a broad correction that accounts for around 58% of the variation (see Figure 4) in the training sample. We discuss in § 5.2 that PC₁ does not correlate by itself with s_{BV} , and therefore the first maximum-light eigenvector likely does not describe variation of a stretch-like prop-

erty of SN Ia light-curves. Instead, it may be correcting for differences in the flux calibration between optical and NIR spectra — if so, the final NIR prediction should be on the appropriate scale of the optical spectrum.

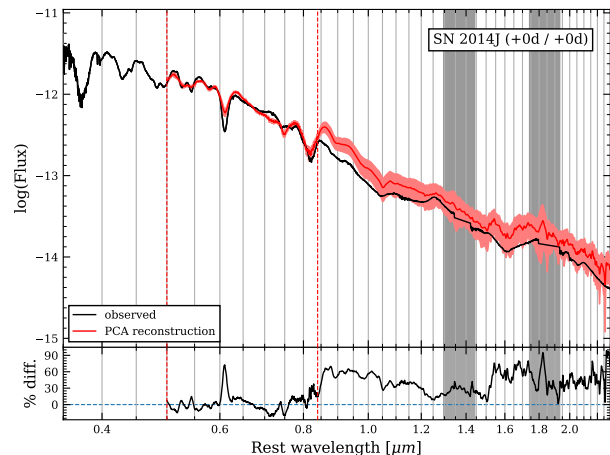


Figure 14. Maximum-light extrapolation for SN 2014J. All formatting is the same as that in Figure 5. Although SN 2014J is classified as a CN SN Ia, a constant offset is prominently seen between the observation and prediction. This may suggest that photometric corrections to spectra are necessary to strengthen the performance of these extrapolations, which requires more photometric observations in both the optical and NIR.

An illustration of this problem is shown in Figure 14, which shows a maximum-light prediction of SN 2014J using a merged optical-NIR spectrum (Galbany et al. 2016; Srivastav et al. 2016) in the same way as those in § 4.2. SN 2014J is known to be highly reddened (Amanullah et al. 2014; Foley et al. 2014). We assume host-galaxy color-excess values of $E(B - V)_{host} = 1.24$ mag and $R_V = 1.44$ (Ashall et al. 2014) to correct the spectrum for extinction using the CCM law (Cardelli et al. 1989), similar to spectra in the PC training data. Even though the merging and prediction process is the same as the other four SNe Ia that yields good fits, the case of SN 2014J is unexpectedly inadequate. Inside the 0.50–0.84 μm region which was projected onto the eigenvectors, the PCA reconstruction fails to fit the observation for most features in this region, and this is especially true for Si II. It seems as though SN 2014J does not exhibit the same behavior as the training sample and therefore could be an interesting case study on its own. It is worth noting that, although we classify SN 2014J as a CN with a probability of 67.6%, it is also on the faster end of CNs with $v_{\text{Si II}}$ of 12.0×10^3 km s⁻¹ and could nearly be considered a BL SN Ia by traditional classification with only pEWs. However, the

GMM probability of belonging to the BL group is 13.5%. It was shown in § 4.2 that this prediction process is not suitable for BLs such as SN 2022hrs, as a constant offset from the prediction was produced. Perhaps the same underlying reasoning is being displayed for the case of SN 2014J. This shows that more observations of BL and faster SNe Ia are needed for a complete understanding of the diversity of SNe Ia.

Similar to SN 2022hrs, SN 2014J shows a large and nearly constant offset seen between the prediction and the observation after $0.84 \mu\text{m}$. Because the observations shown in black are simply merged by scaling the NIR to the red end of the optical flux, there could still be large discrepancies between it and the true SED of the SN Ia, and one would need observed photometry to correct for them. If the first PC were to describe some sort of correction that adjusts the NIR prediction to be on the same true optical scale, then the offset shown in Figure 14 is not a problem with the model, but rather the reference observation. However, it is again difficult to confirm this without observed photometry of the training set of SNe Ia.

Because the differences in the flux calibration between the optical and NIR parts of the training spectra are not completely systematic due to the inhomogeneity of the spectroscopic observations, corrections should still be made to the final predictions. We chose not to do so in § 4 for consistency with the lack of NIR photometric observations. However, it will yield a more accurate SED approximation with correct synthetic photometric colors if observed photometry is available. It is also worth noting that spectroscopic templates that are parameterized by light-curve quantities are also photometry-corrected separately after a first approximation is given to light-curve fitting procedures such as SNooPy.

5.4. Comparison with Templates – Spectroscopy

In this section we provide a brief comparison between the extrapolation procedure described in this work and the parameterized spectral templates of Lu et al. (2023). In short, Lu et al. (2023) makes use of 331 NIR spectra of 94 SNe Ia and performs PCA on multiple regions in wavelength space to create a model that is parameterized by s_{BV} using Gaussian process regression. A substantial statistical comparison of the two methods is not provided here due to the complexity of the predictions and lack of data with which to perform tests.

In Figure 15, the template approximation of SNe 2011fe, 2014J, 2021fxy, and 2021aefx are overlaid on top of the extrapolations shown here in earlier sections. The templates were given the same phase as well as values of s_{BV} for each SN Ia: $s_{\text{BV}} = 0.95$

for SN 2011fe (Ashall et al. 2019), $s_{\text{BV}} = 0.99$ for SN 2021fxy (DerKacy et al. 2023), and $s_{\text{BV}} = 1.05$ for SN 2021aefx (Ni et al. 2023). We also use $s_{\text{BV}} = 1.00$ for SN 2014J by converting its measured value of $\Delta m_{15}(B) = 0.98$ (Li et al. 2019) to s_{BV} using the relation determined by Burns et al. (2018). The template predictions were then scaled to the optical part of the observations in the same way as the NIR observations.

From Figure 15, for SNe 2011fe, 2021fxy, and 2021aefx, the extrapolation and template methods produce similar results overall. This is expected as models for both the extrapolation method and the spectral templates were built using subsets of the same FIRE NIR spectra. In the case of SN 2011fe, the template seems to be more true to the observation, however after $1.5 \mu\text{m}$ both methods deviate significantly from the observation. As this effect is prominently seen in both the extrapolation and the template, this may be the result of the inhomogeneity between the CSP NIR spectra used here and the other observations, rather than the fault of the prediction method itself. Both methods perform well for SN 2021fxy, consistently fitting the observed spectrum in each wavelength region. The fits for SN 2021aefx are inadequate for both methods, but interestingly redward of $1.5 \mu\text{m}$ the extrapolation begins to overestimate the flux, leading to a near-zero difference in integrated flux, whereas the template continues to underestimate the flux. The spectroscopic behavior exhibited by SN 2021aefx and the inability of both the extrapolation and template to reconstruct the observed spectrum may be due to the low GMM probability for SN 2021aefx belonging to the CN Branch group. The probability that it lies within the CN group is only 57.6%, suggesting that it exhibits some Si II and other spectroscopic behavior that is atypical of CNs.

Finally, it is clear that the template prediction is a drastically better fit to the observation of SN 2014J than that given by the extrapolation, even if the extrapolation were to be corrected by a constant factor. This is likely due to the training sample used by Lu et al. (2023) being more representative of SNe Ia similar to SN 2014J and even BLs, as there were far fewer constraints on data selection. It is surprising that the template produces such a good fit to this spectrum, given that SN 2014J seems also atypical for CN SNe Ia as it has such a high value of $v_{\text{Si II}}$. Although these four SNe Ia all exhibit similar values of s_{BV} with $0.95 < s_{\text{BV}} < 1.05$, they each display fairly unique spectroscopic behavior. Because of this, it is also unexpected that the template method seems to perform better overall compared to the extrapolation method, which makes predictions using spectroscopic information instead of the single s_{BV} parameter.

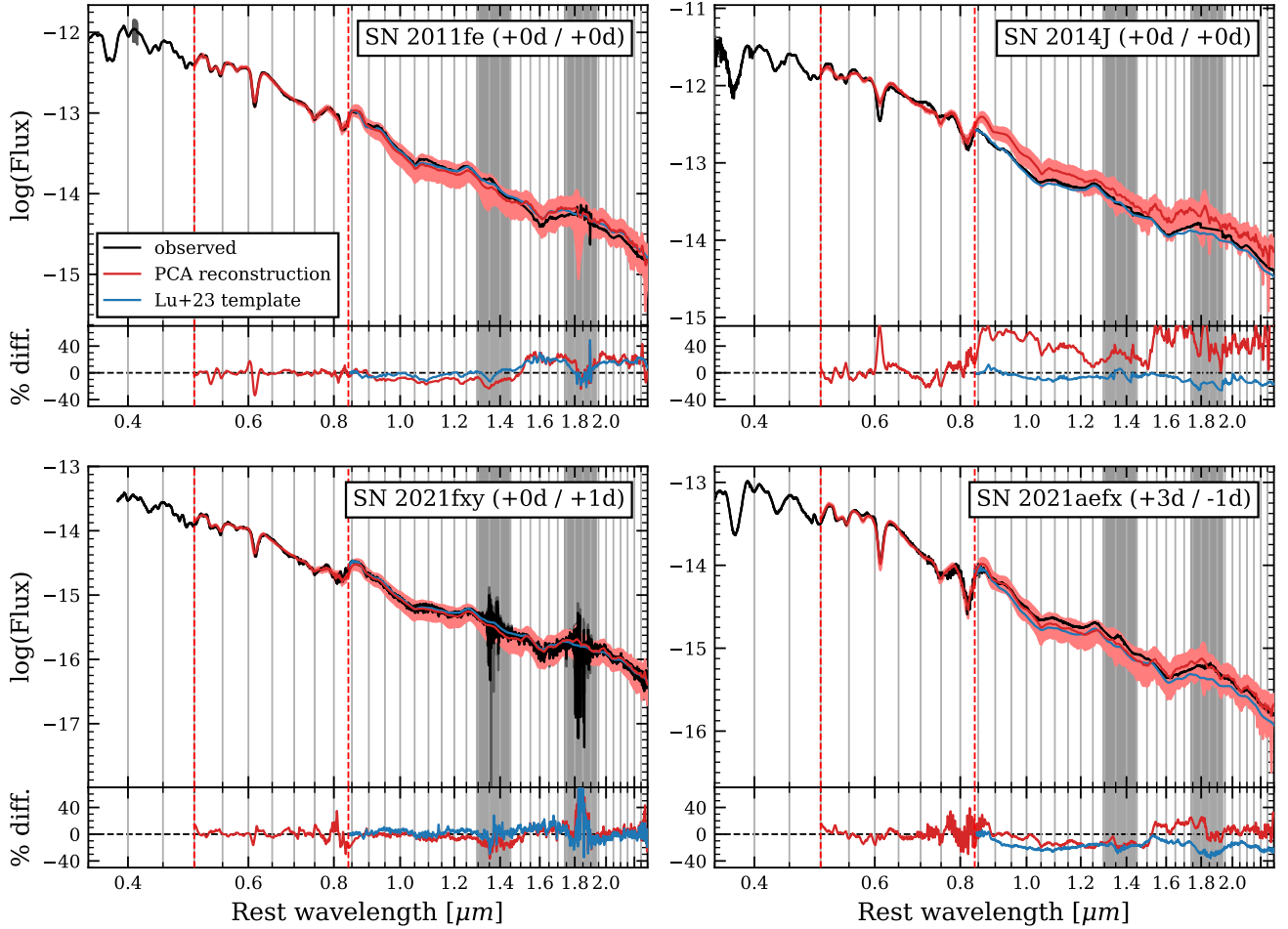


Figure 15. Comparison of near-maximum-light extrapolations of SNe 2011fe, 2014J, 2021fxy, and 2021aefx with Lu et al. (2023) spectral templates given their respective values of s_{BV} and phase.

The likely explanation for this is the much more limited samples sizes used for the extrapolation method, and therefore to improve this method to be consistently on par with spectral templates, more concurrent spectroscopic observations in both the optical and NIR are required.

Because the template method and this extrapolation method both make use of PCA to generate models, a similar sample size of around 100 SNe Ia (rather than the maximum of 34 used here) would likely be sufficient in capturing the spectroscopic information needed in both the optical and NIR to make models that are consistently comparable to the spectral template method. It may be the case that training these models on a comparable sample size of spectra allows the advantages of the extrapolation method to produce better results in some cases. Despite such a drastically smaller sample

size, the extrapolation method does well in rivaling the spectral template results.

5.5. Comparison with Templates – Photometry

Similar to § 5.4, we also provide in this section a comparison between the extrapolation and the spectral templates of Lu et al. (2023) in the context of photometry. In particular, we make this comparison by comparing bolometric light-curves obtained from SNooPy, which has been modified slightly to reflect the procedure discussed below. This comparison is a more realistic and applicable approach to comparing integrated flux as a function of time.

For the same four SNe Ia as in § 5.4 — SNe 2011fe, 2014J, 2021fxy, and 2021aefx — we calculate the bolometric light-curves of each SN Ia in the following way. First, we gather BVR photometry of SN 2011fe (Richmond & Smith 2012), BVR photometry of SN 2014J

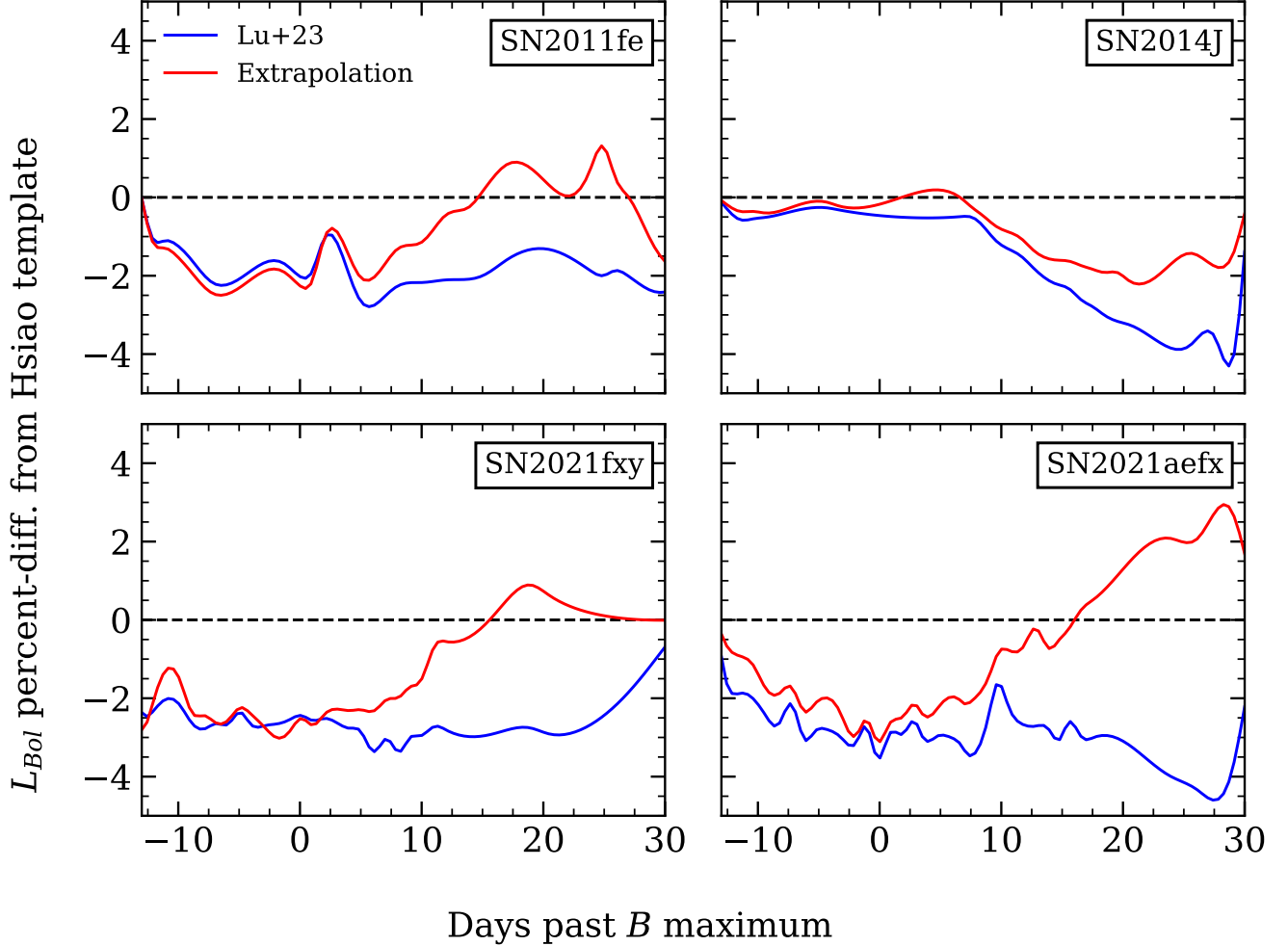


Figure 16. Percent-difference of calculated L_{Bol} light-curves from using the Hsiao et al. (2007) template for the method presented in this work (Extrapolation) and for the Lu et al. (2023) (NIR) template. Note that the Hsiao et al. (2007) template does not yield light-curves taken as truth, but rather it is used as a reference to compare the two other methods.

(Foley et al. 2014), $uBVgri$ photometry of SN 2021fxy (DerKacy et al. 2023), and $BVgri$ photometry of SN 2021aefx (Hosseinzadeh et al. 2022). This photometry allows for a measurement of s_{BV} using SNooPy’s `EBV_model2` which in turn is able to produce an approximate SED from the spectral templates of Hsiao et al. (2007), which we will henceforth refer to as the Hsiao templates, that are built into SNooPy. From here, three different methods are used to determine bolometric light-curves for each SN Ia: the default SNooPy method, which integrates the Hsiao templates to calculate the bolometric luminosity (L_{Bol}); the extrapolation method, which does the same with the extrapolation procedure discussed in this work; and the NIR template method, which again does the same, but using the spectral template of Lu et al. (2023). For clarification, we emphasize that L_{Bol} is calculated by integrating an estimated SED as opposed to using the aforementioned

photometric observations of the four SNe Ia with differing bands available. The listed photometry is primarily used to determine s_{BV} , which parameterizes the spectral templates, which are then integrated to achieve L_{Bol} .

For the extrapolation and NIR template methods, the Hsiao template is used in the optical regime until the red-most wavelength in the effective range of the red-most band of the photometry given. For example, this is about 9000 Å when BVR photometry is given. Redward of this wavelength, either the extrapolation or NIR template method replaces the Hsiao template by merging the SEDs between 8750–9250 Å. For the extrapolation method, the optical part of the Hsiao template is treated as an observation and projected onto the relevant eigenvectors so that a prediction can be made. This is necessary for testing purposes as an observed spectrum of each supernova is not available for each epoch that L_{Bol} is calculated. After the full optical+NIR SED

is approximated, it follows the same process in SNooPy by correcting for the observed photometry provided and then computing the bolometric luminosity.

The three bolometric light-curves for each SN Ia were calculated between -16 and $+30$ days relative to B -maximum, and, for the purpose of comparison, the percent-difference of L_{Bol} given the extrapolation and NIR template methods from that of the Hsiao templates is shown in Figure 16. Note that the Hsiao templates and their resulting light-curves are not taken as truth, and this difference is displayed to give them a shared point of reference. From Figure 16 we see that in L_{Bol} space, the two SED estimation methods yield very similar light-curves between around -16 to $+10$ days until they begin to deviate consistently for each SN Ia. After $+10$ days the extrapolation method yields around $+2\%$ or higher bolometric luminosity than the NIR templates when compared to the Hsiao templates. This could be due to the lower sample sizes available at later times for the extrapolation method (see Figure 2).

Finally, it is worth noting that, although the extrapolated spectrum of SN 2014J exhibits sizable offset from the NIR template (seen in Figure 15), the bolometric light-curves show very small differences between the SED estimates around maximum light. This is likely caused by differences between the spectrum used to generate the extrapolation shown in Figure 15 and the optical part of the Hsiao template used to generate the extrapolations that yield light-curves from Figure 16. In addition, the merging process occurs in different wavelength regions. Therefore, there are no real inconsistencies in what is seen between Figure 15 and Figure 16. Ultimately, we find that the two methods yield very similar results in both maximum-light spectroscopy and bolometric luminosity surrounding maximum light. Most differences that occur between the two methods are at times later than $+10$ days where sample sizes are smaller, leading to a less representative sample of the population of SNe Ia with which to train models.

6. CONCLUSIONS

In this study, we make use of optical spectra alongside NIR FIRE spectra from the CSP I & II data set to study correlations between optical and NIR spectroscopy in an attempt to model optical-NIR behavior using PCA. This differs from spectral template methods as this method is not intrinsically parameterized by s_{BV} or other stretch-like quantities, as s_{BV} does not capture the full diversity of SNe Ia in the NIR regime. It is shown here that using patterns exhibited by SN Ia spectra to extrapolate these spectra into the NIR up to $2.3 \mu\text{m}$ results in predictions that are in accordance with observations. Our results

show absolute differences typically of 3% or less in integrated flux from observations, although this may vary greatly depending on the supernova, as is evident from the SN 2014J trial. In cases such as this one, we find that there are large offsets between extrapolated flux and observed flux. These offsets may be due to differences in the flux calibrations between optical and NIR spectra that are unaccounted for in this study. This problem may be addressed by correcting both training and testing spectra by matching the colors of the synthetic photometry and observed photometry at concurrent phases. This as well as large uncertainties shown for these extrapolations clearly illustrates the need for more observations to train these data-informed models. Specifically, the importance of *concurrent* optical and NIR spectroscopy cannot be overstated for the study of SNe Ia at early phases due to the variation in their spectra at these times.

We also find that Si II plays a significant role in partially explaining the diversity of NIR SN Ia spectroscopy, which may be expected given the well-studied (Branch et al. 2006) classification system. Performing the extrapolation process given only Si II information results in similar and sometimes better fits to observations than using a wider range of optical spectra. In addition, projecting Si II onto the set of maximum-light eigenvectors gives a set of projection values that are shown to contain information that is similar to a supernova’s Branch classification, however they also contain Si II velocity information as well. This velocity information may be useful in explaining the dispersion seen in the Si II $\lambda 6355$ pEW-velocity relation that leads to such high-velocity CN SNe Ia. These projections or a similar quantity may be good candidates to replace pEW measurements, as obtaining pEWs can be inconsistent, since they are easily contaminated due to line blending. It is also seen that these projections extract the SNooPy measurement of s_{BV} well from a simple linear model, within a spread of about ± 0.1 units. Interestingly, this provides a method of predicting the photometric s_{BV} for a SN Ia given only a maximum-light spectrum, therefore the maximum-light PCs contain enough information to sub-categorize SNe Ia. The photometric quantity s_{BV} is obtained roughly over the first 30 days from the B and V light curves. Nevertheless, a single maximum-light spectrum contains enough information to estimate s_{BV} to an accuracy of $\sim 10\%$, indicating that the maximum light spectrum contains the explosion history of the ejecta. This shows the complementarity of spectroscopy and photometry for understanding complex astrophysical phenomena.

Finally, we compare this extrapolation method to the NIR templates of Lu et al. (2023) and find that, although the two yield similar results for practical purposes, the NIR templates still have an edge on extrapolation. NIR templates give SED approximations that were slightly closer to observation in most cases. In one case shown here, the study of SN 2014J, the NIR template was much closer to the observation. It is also seen that, when applied to bolometric light-curves, these two methods produce consistently similar light-curves between around -16 to $+10$ days relative to maximum light. We speculate that, with additional data added to the training sample, this method could indeed be capable of fitting to NIR spectroscopic observations of SNe Ia that contain fundamental differences that are independent of light-curve shape. This is because we have shown that projections onto the PCs determined here appear to have some relationship with s_{BV} and spectroscopic quantities such as Si II pseudo-equivalent widths and Si II $\lambda 6355$ velocity. We surmise that, if future observations allow for a comparable sample size as that used by Lu et al. (2023) ($N \sim 100$), the flexibility of this non-parametric extrapolation method may allow for improvements compared to the spectral template in some cases. It offers a solution to the fact that NIR light-curves, especially around the secondary maximum, cannot be parameterized by s_{BV} ; with more data, this can be tested more completely. This method is limited by the data available, but it is shown here to have potential in predicting the NIR behavior of SNe Ia.

This extrapolation method along with precalculated time-dependent eigenvectors is openly maintained in the software package named SNeX (Burrow 2024). This software takes a spectrum as input, and with user-defined parameters such as phase and the projection region itself, the spectrum is projected onto a set of eigenvectors to produce the resulting linear combination spectrum. There are many variables in the work described here, many of which were assumed in this paper for simplicity and not studied in detail. Therefore, some parameters may yield better results when changed for certain SNe Ia, which could be the subject of future work when a more extensive training data sample is established.

7. ACKNOWLEDGMENTS

A.B., E.B., P.B., and P.H. acknowledge support from NASA grant 80NSSC20K0538. E.B., C.A., J.D., and P.H. acknowledge support from NASA grants JWST-GO-02114, JWST-GO-02122, JWST-GO-04522, JWST-GO-04217, and JWST-GO-04436. Support for programs #2114, #2122, #4522 #4217, and #4436

were provided by NASA through a grant from the Space Telescope Science Institute, which is operated by the Association of Universities for Research in Astronomy, Inc., under NASA contract NAS 5-03127. E.B., C.A., and J.D. acknowledge support from HST-AR-17555, Support for Program number 17555 was provided through a grant from the STScI under NASA contract NAS5-26555. J.L. acknowledges support from NSF grant AAG-2206523. L.G. acknowledges financial support from the Spanish Ministerio de Ciencia e Innovación (MCIN), the Agencia Estatal de Investigación (AEI) 10.13039/501100011033, and the European Social Fund (ESF) "Investing in your future" under the 2019 Ramón y Cajal program RYC2019-027683-I and the PID2020-115253GA-I00 HOSTFLOWS project, from Centro Superior de Investigaciones Científicas (CSIC) under the PIE project 20215AT016, and the program Unidad de Excelencia María de Maeztu CEX2020-001058-M, and from the Departament de Recerca i Universitats de la Generalitat de Catalunya through the 2021-SGR-01270 grant. M.D. Stritzinger is funded by the Independent Research Fund Denmark (IRFD, grant number 10.46540/2032-00022B). Some of the calculations presented here were performed at the National Energy Research Supercomputer Center (NERSC), which is supported by the Office of Science of the U.S. Department of Energy under Contract No. DE-AC03-76SF00098, at the Höchstleistungs Rechenzentrum Nord (HLRN), and at the OU Supercomputing Center for Education & Research (OSCER) at the University of Oklahoma (OU). We thank all these institutions for a generous allocation of computer time.

Software: SNeX (Burrow 2024), EMPCA (Bailey 2012), SNooPy (Burns et al. 2011), Spextractor (Burrow et al. 2020), scikit-learn (version 0.22.2, Pedregosa et al. 2011), NumPy (version 1.18.2, Oliphant 2006; van der Walt et al. 2011), Matplotlib (version 3.2.1, Hunter 2007)

REFERENCES

- Amanullah, R., Goobar, A., Johansson, J., et al. 2014, *ApJ*, 788, L21, doi: [10.1088/2041-8205/788/2/L21](https://doi.org/10.1088/2041-8205/788/2/L21)
- Ashall, C., Mazzali, P., Bersier, D., et al. 2014, *MNRAS*, 445, 4427, doi: [10.1093/mnras/stu1995](https://doi.org/10.1093/mnras/stu1995)
- Ashall, C., Hsiao, E. Y., Hoefflich, P., et al. 2019, *ApJ*, 875, L14, doi: [10.3847/2041-8213/ab1654](https://doi.org/10.3847/2041-8213/ab1654)
- Bailey, S. 2012, *PASP*, 124, 1015, doi: [10.1086/668105](https://doi.org/10.1086/668105)
- Baron, E., Bongard, S., Branch, D., & Hauschildt, P. H. 2006, *ApJ*, 645, 480, doi: [10.1086/504101](https://doi.org/10.1086/504101)
- Branch, D., Dang, L. C., Hall, N., et al. 2006, *PASP*, 118, 560
- Brout, D., Sako, M., Scolnic, D., et al. 2019a, *ApJ*, 874, 106, doi: [10.3847/1538-4357/ab06c1](https://doi.org/10.3847/1538-4357/ab06c1)
- Brout, D., Scolnic, D., Kessler, R., et al. 2019b, *ApJ*, 874, 150, doi: [10.3847/1538-4357/ab08a0](https://doi.org/10.3847/1538-4357/ab08a0)
- Burns, C., Hsiao, E., Suntzeff, N., et al. 2021, *The Astronomer's Telegram*, 14441, 1
- Burns, C. R., Stritzinger, M., Phillips, M. M., et al. 2011, *AJ*, 141, 19, doi: [10.1088/0004-6256/141/1/19](https://doi.org/10.1088/0004-6256/141/1/19)
- . 2014, *ApJ*, 789, 32, doi: [10.1088/0004-637X/789/1/32](https://doi.org/10.1088/0004-637X/789/1/32)
- Burns, C. R., Parent, E., Phillips, M. M., et al. 2018, *ApJ*, 869, 56, doi: [10.3847/1538-4357/aae51c](https://doi.org/10.3847/1538-4357/aae51c)
- Burrow, A. 2024, *anthonyburrow/SNEx: v1.0.0: First release, 1.0.0*, Zenodo, doi: [10.5281/zenodo.10849861](https://doi.org/10.5281/zenodo.10849861)
- Burrow, A., Baron, E., Ashall, C., et al. 2020, *ApJ*, 901, 154, doi: [10.3847/1538-4357/abafa2](https://doi.org/10.3847/1538-4357/abafa2)
- Cardelli, J. A., Clayton, G. C., & Mathis, J. S. 1989, *ApJ*, 345, 245, doi: [10.1086/167900](https://doi.org/10.1086/167900)
- DerKacy, J. M., Baron, E., Branch, D., et al. 2020, *ApJ*, 901, 86, doi: [10.3847/1538-4357/abae67](https://doi.org/10.3847/1538-4357/abae67)
- DerKacy, J. M., Paugh, S., Baron, E., et al. 2023, *MNRAS*, 522, 3481, doi: [10.1093/mnras/stad1171](https://doi.org/10.1093/mnras/stad1171)
- Folatelli, G., Phillips, M. M., Burns, C. R., et al. 2010, *AJ*, 139, 120, doi: [10.1088/0004-6256/139/1/120](https://doi.org/10.1088/0004-6256/139/1/120)
- Foley, R. J., Fox, O. D., McCully, C., et al. 2014, *MNRAS*, 443, 2887, doi: [10.1093/mnras/stu1378](https://doi.org/10.1093/mnras/stu1378)
- Friesen, B., Baron, E., Wisniewski, J. P., et al. 2014, *ApJ*, 792, 120, doi: [10.1088/0004-637X/792/2/120](https://doi.org/10.1088/0004-637X/792/2/120)
- Galbany, L., Moreno-Raya, M. E., Ruiz-Lapuente, P., et al. 2016, *MNRAS*, 457, 525, doi: [10.1093/mnras/stw026](https://doi.org/10.1093/mnras/stw026)
- Guy, J., Astier, P., Baumont, S., et al. 2007, *A&A*, 466, 11, doi: [10.1051/0004-6361:20066930](https://doi.org/10.1051/0004-6361:20066930)
- Hamuy, M., Phillips, M. M., Suntzeff, N. B., et al. 1996, *AJ*, 112, 2398
- Hoefflich, P. 2017, in *Handbook of Supernovae*, ed. A. W. Alsabti & P. Murdin, 1151, doi: [10.1007/978-3-319-21846-5_56](https://doi.org/10.1007/978-3-319-21846-5_56)
- Hosseinzadeh, G., Sand, D. J., Lundqvist, P., et al. 2022, *ApJ*, 933, L45, doi: [10.3847/2041-8213/ac7cef](https://doi.org/10.3847/2041-8213/ac7cef)
- Hsiao, E. Y., Conley, A., Howell, D. A., et al. 2007, *ApJ*, 663, 1187, doi: [10.1086/518232](https://doi.org/10.1086/518232)
- Hsiao, E. Y., Phillips, M. M., Marion, G. H., et al. 2019, *PASP*, 131, 014002, doi: [10.1088/1538-3873/aae961](https://doi.org/10.1088/1538-3873/aae961)
- Hsiao, Y. C. E. 2009, PhD thesis, University of Victoria, Canada
- Hunter, J. D. 2007, *Computing in Science and Engineering*, 9, 90, doi: [10.1109/MCSE.2007.55](https://doi.org/10.1109/MCSE.2007.55)
- Jha, S. W., Maguire, K., & Sullivan, M. 2019, *Nature Astronomy*, 3, 706, doi: [10.1038/s41550-019-0858-0](https://doi.org/10.1038/s41550-019-0858-0)
- Kenworthy, W. D., Jones, D. O., Dai, M., et al. 2021, *ApJ*, 923, 265, doi: [10.3847/1538-4357/ac30d8](https://doi.org/10.3847/1538-4357/ac30d8)
- Krisciunas, K., Contreras, C., Burns, C. R., et al. 2017, *AJ*, 154, 211, doi: [10.3847/1538-3881/aa8df0](https://doi.org/10.3847/1538-3881/aa8df0)
- Kwok, L. A., Jha, S. W., Temim, T., et al. 2023, *ApJ*, 944, L3, doi: [10.3847/2041-8213/acb4ec](https://doi.org/10.3847/2041-8213/acb4ec)
- Li, W., Wang, X., Hu, M., et al. 2019, *ApJ*, 882, 30, doi: [10.3847/1538-4357/ab2b49](https://doi.org/10.3847/1538-4357/ab2b49)
- Lu, J., Hsiao, E. Y., Phillips, M. M., et al. 2023, *ApJ*, 948, 27, doi: [10.3847/1538-4357/acc100](https://doi.org/10.3847/1538-4357/acc100)
- Maoz, D., Mannucci, F., & Nelemans, G. 2014, *ARA&A*, 52, 107, doi: [10.1146/annurev-astro-082812-141031](https://doi.org/10.1146/annurev-astro-082812-141031)
- Mazzali, P. A., Sullivan, M., Hachinger, S., et al. 2014, *MNRAS*, 439, 1959, doi: [10.1093/mnras/stu077](https://doi.org/10.1093/mnras/stu077)
- Ni, Y. Q., Moon, D.-S., Drout, M. R., et al. 2023, *ApJ*, 959, 132, doi: [10.3847/1538-4357/ad0640](https://doi.org/10.3847/1538-4357/ad0640)
- Oke, J. B., & Sandage, A. 1968, *ApJ*, 154, 21, doi: [10.1086/149737](https://doi.org/10.1086/149737)
- Oliphant, T. E. 2006, *A guide to NumPy (USA: Trelgol Publishing)*
- Papadogiannakis, S., Dhawan, S., Morosin, R., & Goobar, A. 2019, *MNRAS*, 485, 2343, doi: [10.1093/mnras/stz493](https://doi.org/10.1093/mnras/stz493)
- Pearson, K. 1901, *The London, Edinburgh, and Dublin Philosophical Magazine and Journal of Science*, 2, 559, doi: [10.1080/14786440109462720](https://doi.org/10.1080/14786440109462720)
- Pedregosa, F., Varoquaux, G., Gramfort, A., et al. 2011, *Journal of Machine Learning Research*, 12, 2825, doi: <http://jmlr.org/papers/v12/pedregosa11a.html>
- Perlmutter, S., Aldering, G., Goldhaber, G., et al. 1999, *ApJ*, 517, 565, doi: [10.1086/307221](https://doi.org/10.1086/307221)
- Phillips, M. M. 1993, *ApJ*, 413, L105
- Phillips, M. M., Lira, P., Suntzeff, N. B., et al. 1999, *AJ*, 118, 1766
- Phillips, M. M., Contreras, C., Hsiao, E. Y., et al. 2019, *PASP*, 131, 014001, doi: [10.1088/1538-3873/aae8bd](https://doi.org/10.1088/1538-3873/aae8bd)
- Richmond, M. W., & Smith, H. A. 2012, *JAAVSO*, 40, 872, doi: [10.48550/arXiv.1203.4013](https://doi.org/10.48550/arXiv.1203.4013)
- Riess, A. G., Press, W. H., & Kirshner, R. P. 1996, *ApJ*, 473, 88

- Riess, A. G., Filippenko, A. V., Challis, P., et al. 1998, *AJ*, 116, 1009, doi: [10.1086/300499](https://doi.org/10.1086/300499)
- Roweis, S. 1997, in *Advances in Neural Information Processing Systems 10 (NIPS 1997)*, ed. M. Jordan, M. Kearns, & S. Solla.
https://papers.nips.cc/paper_files/paper/1997/hash/d9731321ef4e063ebbee79298fa36f56-Abstract.html
- Saunders, C., Aldering, G., Antilogus, P., et al. 2018, *ApJ*, 869, 167, doi: [10.3847/1538-4357/aaec7e](https://doi.org/10.3847/1538-4357/aaec7e)
- Schlafly, E. F., & Finkbeiner, D. P. 2011, *ApJ*, 737, 103, doi: [10.1088/0004-637X/737/2/103](https://doi.org/10.1088/0004-637X/737/2/103)
- Srivastav, S., Ninan, J. P., Kumar, B., et al. 2016, *MNRAS*, 457, 1000, doi: [10.1093/mnras/stw039](https://doi.org/10.1093/mnras/stw039)
- Stritzinger, M. D., Holmbo, S., Morrell, N., et al. 2023, *A&A*, 675, A82, doi: [10.1051/0004-6361/202243376](https://doi.org/10.1051/0004-6361/202243376)
- Tripp, R. 1998, *A&A*, 331, 815
- van der Walt, S., Colbert, S. C., & Varoquaux, G. 2011, *Computing in Science and Engineering*, 13, 22, doi: [10.1109/MCSE.2011.37](https://doi.org/10.1109/MCSE.2011.37)
- Yarbrough, Z., Baron, E., DerKacy, J. M., et al. 2023, *MNRAS*, 521, 3873, doi: [10.1093/mnras/stad758](https://doi.org/10.1093/mnras/stad758)